Engineering Structures 80 (2014) 40–52

Contents lists available at ScienceDirect

Engineering Structures

journal homepage: www.elsevier.com/locate/engstruct

# Plasticity based approach for failure modelling of unreinforced masonry

Nitin Kumar [a], Amirtham Rajagopal [a,*], Manoj Pandey [b]

[a] Department of Civil Engineering, Indian Institute of Technology Hyderabad, Andhra Pradesh, India
[b] Department of Mechanical Engineering, Indian Institute of Technology Madras, Tamil Nadu, India

ARTICLE INFO

*Article history:*
Received 30 May 2013
Revised 7 August 2014
Accepted 12 August 2014

*Keywords:*
Masonry modelling
Plasticity
Composite interface model
Failure criteria

ABSTRACT

In this work, a plasticity based composite interface model is proposed for failure analysis of unreinforced masonry. The hyperbolic composite interface model consists of a single surface yield criterion, which is a direct extension of Mohr-Coulomb criteria with cut in tension region and a cap in compression region. The inelastic behaviour includes potential crack, slip, and crushing of the masonry joints. A micro mechanical based approach is adopted for failure modelling of the masonry. The model is developed by using a fully implicit backward-Euler integration strategy. It is combined with a local/global Newton solver, based on a consistent tangent operator compatible with an adaptive sub stepping strategy. The model is implemented in standard finite element software (ABAQUS) by using user defined subroutine and verification is conducted in all its basic modes. Finally, the model is validated by comparing with experimental results available in the literature.



## 1. Introduction

Masonry is a heterogeneous anisotropic continuum; made up of the brick and mortar arranged in a periodic or non periodic manner. In particular, the inhomogeneity is due to the different mechanical properties of its constituents, and the anisotropy is due to the different masonry patterns, that can be obtained by variation of geometry, nature and arrangement of mortar and brick. The behaviour of masonry is very complex and highly non-linear due to the behaviour of its constituents, which are quasi-brittle in nature and have a large difference in their stiffness. It represents a very particular mechanical behaviour, which is primarily due to the lack of homogeneity and standardization (see [1,2]). The structural response of such a composite material derives from the complex interaction between its constituents. Under the in-plane loading, masonry is subjected to a biaxial state of stress and thus masonry constituents may fail in individual or combined mechanisms (see [3–6]). These failure mechanism are used in micro modelling of masonry to understand its behaviour.

Many computational studies have been carried out at various scales to understand and simulate the behaviour of masonry. The modelling of masonry at different scales depends up on the level of accuracy and simplicity desired. This includes micro-modelling and macro-modelling. In micro-modelling, the unit and mortar are represented by continuum elements and unit-mortar interface is represented by a discontinuous interface element. This detailed micro-modelling procedure leads to very accurate results, but requires an intensive computational effort. This drawback can be partially overcome in simplified micro-modelling, by making an assumption that mortar and two unit-mortar interface is lumped into a joint between expended units. The units are expended in order to keep the geometry of structure unchanged. The computational cost of simplified micro-model can be further reduced, by replacing expanded units by the rigid element. Using rigid elements decreases the number of degrees of freedom, which consequently reduces the computational time. In macro-modelling, masonry is considered as a composite, which does not make any distinction between units and joints. The material is regarded as a fictitious homogeneous anisotropic continuum.

## 2. Literature review

There has been several experimental studies reported in literature for understanding behaviour of the masonry for instance (see [7–12]). Masonry exhibits a quasi-brittle behaviour due to its constituents, thus failure analysis of a masonry structure abides in the realistic modelling of the fractures and associated softening behaviour. Therefore modelling techniques of masonry are analogous to that developed in concrete and rock mechanics. Many plasticity based constitutive models have been proposed in the recent years that can simulate initiation and propagation of crack under combined normal and shear stresses [13–18].

* Corresponding author.
*E-mail address:* rajagopal@iith.ac.in (R. Amirtham).

http://dx.doi.org/10.1016/j.engstruct.2014.08.021
0141-0296/

Aryan and Hegemier [19], Page [20] made early attempts to study the masonry failure using simplified micro modelling. Stankowski et al. [21,22] proposed a plasticity based constitutive model to describe the fracture and slip of the interface in cementitious materials. This model uses a curvilinear Mohr-Coulomb yield function with a tension cut-off and the yield function has a smooth transition between shear and tension region. They considered the tensile strength softening without changing shape of yield function (i.e. degradation of tensile strength is considered whereas cohesion and friction angle are considered to be unchanged). Lotfi et al. [23,24] have developed an interface model that incorporates additional softening mechanisms i.e. the degradation of cohesion and friction angle with additional attention being paid to include the dilatancy. The models presented there can simulate initiation and propagation of crack under combined normal and shear stresses in tension-shear and compression-shear region. However, it fails to simulate masonry under high compression stress. Lourenço [25–27] introduced multi-surface interface model for analysis of masonry structures. The constitutive model is illustrated by three yield functions: a tension cut-off for mode-I failure, a Mohr-Coulomb failure envelope for mode-II failure and a cap model for compressive failure. The model is capable of simulating masonry under tension-shear, compression-shear and even under high compression stress. Due to presence of three yield criteria, singularity problem arises at the non-smooth corner in transition zone from tension to shear and shear to compression. Many other plasticity based constitutive model have also been proposed in recent years. Giambanco et al. [28] presented an interface model suitable to simulate the behaviour of mortar joint in the masonry, using the Mohr-Coulomb bilinear limit surface with tension-cut off. The model considers the softening response that occurs, along with decohesion process in the presence of shear and tension. Oliveira and Lourenco [29,30] extended the Lourenco and Rots model to damage formulation for simulating the cyclic behaviour of interface element. Dolatshahi et al. [31] used the Lourenco and Rots model and have shown that in a computational scheme, the use of rigid elements along with non-linear line interfaces leads to a reduced number of degrees-of-freedom, which consequently reduces the computational time. Dhanasekar et al. [32] carried out explicit finite element analysis of wide spaced reinforced masonry shear wall. The wall is modelled using macroscopic material characteristics for the unreinforced masonry panels and damaged concrete plasticity for the grouted cores containing reinforcement. Anand et al. [33] did a finite element failure analysis of composite masonry walls subjected to both vertical and horizontal loads. It is shown that cracking in the collar joint is initiated at a much smaller magnitude of the horizontal inplane load compared to the vertical load.

There has been interesting works on understanding the failure modes of solid brick masonry under in-plane loading (see [34]) and numerical modelling of masonry using finite element method [20] for understanding the behaviour of columns under horizontal loads [35], and under cyclic loads [36]. There has also been some other works on 3D analysis of masonry columns under cyclic loading [37], 3D analysis of masonry columns with grouted reinforcement under cyclic loading [38]. The study on masonry wall under inplane loading [39,40], masonry wall under monotonic loading [41], and masonry wall subjected to seismic loading [42,4] are notable.

There has been very recent works on nonlinear analysis of masonry structures [43]. An equilibrated macro element for nonlinear analysis of masonry structures [44] has been developed for understanding the in plane structural response of masonry panels under lateral loading [45]. Understanding nonlinear behaviour of masonry has been attempted at various scales. A coarse scale model in the context of assumed stress formulation has been implemented in [46] with non associative plasticity. Several mesoscale modelling approaches [47] has been developed for modelling nonlinear behaviour of masonry [48]. A mesoscale cohesive crack model to simulate cyclic behaviour of concrete and masonry structures was presented in [49]. A nonlinear finite element modelling of reinforced masonry shear walls for bidirectional loading response was made in [50]. Similar nonlinear finite element analysis was made to understand the out of plane behaviour of masonry walls with and without CFRP reinforcement in [51]. Ref. [52] have studied the influence of boundary conditions and size effects on the drift capacity of unreinforced masonry walls. Numerical investigation on the influence of FRP retrofit layout and geometry on the inplane behaviour of masonry walls was done by Gian et al. [53]. A new discrete element model for the evaluation of the seismic behaviour of unreinforced masonry buildings has been made by Ivo et al. [54]. Amaryllis et al. [55] have proposed methodology for identification of suitable limit states from nonlinear dynamic analyses of masonry structures.

There has been very recent works to understand the inplane and out of plane behaviour of masonry walls subjected to cyclic loading. A three dimensional cyclic meso-scale numerical procedure for simulation of unreinforced masonry structures is developed in [56]. Nebojsa et al. have undertook a study on modelling the behaviour of seismically strengthened masonry walls subjected to cyclic in-plane shear [57]. Medeiros et al. [58] developed a numerical modelling of non- confined and confined masonry walls. An explicit finite element analysis for the in-plane cyclic behaviour of unreinforced masonry structures was made in [59]. Manos et al. studied the behaviour of masonry assemblages and masonry infilled reinforced concrete frames subjected to combined vertical and cyclic horizontal seismic type loading [60]. Analytical models for cyclic compressive behaviour of brick masonry have also been proposed [61]. In plane cyclic behaviour of masonry walls jacketed with fibre reinforced mortar and fibre grids was made by Viorel et al. [62]. There has also been some recent works on behaviour of masonry walls under combined loadings [63].

The recent advances in computational modelling of masonry structures has been towards understanding their behaviour under cyclic or seismic loads. A comparative analysis on the seismic behaviour of unreinforced masonry buildings with flexible diaphragms was made in [64]. Unreinforced and confined masonry buildings in seismic regions: Validation of macro element models and cost analysis was done in [65]. An equivalent frame model for the nonlinear seismic analysis of masonry buildings was developed in [66]. A seismic vulnerability index for confined masonry shear wall buildings and a relationship with the damage has recently been studied in [67]. Modelling and analysis of time dependent behaviour of historical masonry under high stress loads is presented in [68]. A new discrete element model for the evaluation of seismic behaviour of unreinforced masonry buildings is presented in [69]. Parametrical study of unreinforced flayed masonry walls subjected to horizontal loading through numerical modelling is made in [70].

Structural analysis of a multi-span railway masonry bridge combining in-situ observations, laboratory tests and damage modelling was done in [71]. Effect of in-plane damage on out of plane strength of unreinforced masonry walls was presented in [72]. Modelling of masonry of infilled frames with respect to cracking and damage is presented in [73]. Performance evaluation of masonry in-filled frames under cyclic loading based on damage method has been presented in [74]. A simplified homogenisation based discrete element model for the non-linear static analysis of masonry walls subjected to out-of-plane loaded has been presented in [75].

There has been several other recent works on numerical modelling of masonry structures with structural strengthening using

Fibre Reinforced Polymers (FRP) [76]. Numerical analysis of fibre reinforced polymer retrofitted masonry panels is made in [77]. A combined finite discrete element analysis of dry stone masonry structures was made in [78]. An equilibrated macro-element for non-linear analysis of masonry structures was developed in [79]. Evaluation of different computational modelling strategies for the analysis of low strength masonry structures was made in [80]. Modelling the failure of thin layered mortar joints in masonry was done in [81].

The objective of the paper is to propose plasticity based composite interface model by using a single surface yield criteria, to overcome singularity at the corner region. The composite interface model has been written using the user defined subroutine in commercial software ABAQUS to perform a numerical analysis. In the following section, after demonstrating prominent failure mechanism of masonry, elastic and plastic behaviour of model is described. Then, numerical algorithm is prepared and verified by using basic examples. Finally, the robustness of the proposed model has been assessed by using the results of well-documented experimental work, and the conclusions are made.

## 3. Masonry failure mechanism

In the present study, simplified micro-modelling is adopted to model the masonry. In this approach, the mortar and two adjacent unit-mortar interface is lumped into a joint between expanded units. The units are expanded in order to keep the geometry of structure unchanged, see Fig. 1. The joint is represented by discontinuous interface element, which includes all the inelastic property of the masonry. The inelastic behaviour is due to a potential crack, potential slip and crushing plane. Thus masonry is represented as set of elastic blocks bounded by the potential crack, slip and crushing planes. It is important to develop an accurate model, that must consider all the failure mechanisms that characterise the masonry behaviour.

Many failure mechanism are possible, amongst which the prominent ones are [26,27,4–6] (a) cracking of unit in direct tension, (b) cracking of mortar joint, (c) bed or head joint failure at low value of normal stress, (d) diagonal tension cracking of the unit, (e) masonry crushing. The failure mechanism are shown in Fig. 2. where (a) is unit mechanism, (b) and (c) are the joint mechanism and (d) and (e) are the combine mechanism. An accurate masonry model must include all these failure mechanisms.

## 4. The composite interface model

The composite interface model is used to represent the mechanical behaviour of discontinuous interface element for joint interface in the masonry modelling, which includes potential crack, slip, and crushing planes. In the following section, a complete description of numerical implementation of a plasticity based composite interface model is explained.

### 4.1. Elastic behaviour

The interface elements allows the discontinuity in the displacement field and their behaviour is described by relation between traction force and relative displacement of the interface element. The generalised stress-strain relation can be written in standard form as

$$\boldsymbol{\sigma} = \boldsymbol{K}\boldsymbol{\epsilon} \tag{1}$$

In a 2D framework, $\boldsymbol{\sigma} = \{\sigma_{nn}, \sigma_{tt}\}^T, \boldsymbol{\epsilon} = \{\epsilon_{nn}, \epsilon_{tt}\}^T$ and $\boldsymbol{K} = diag\{k_{nn}, k_{tt}\}^T$ where $nn$ and $tt$ designate normal and tangential components. For simplifying the model, the effect of Poisson's ratio is assumed to be negligible. The Poisson's ratio of the brick is considerably lower than mortar, and most of the behaviour of the masonry is governed by joint mechanics, mortar mechanism and splitting of the brick, thus this assumption seems to be valid. Due to lager difference in the thickness of the mortar and unit, the units are assumed to be linear-elastic. The component of elastic stiffness matrix $\boldsymbol{K}$ can be written as

$$\frac{1}{k_{nn}} = \frac{1}{h_m}\left(\frac{1}{E_u} + \frac{1}{E_m}\right) \tag{2}$$

$$\frac{1}{k_{tt}} = \frac{1}{h_m}\left(\frac{1}{G_u} + \frac{1}{G_m}\right) \tag{3}$$

where $E_u, E_m, G_u$ and $G_m$ are the elastic Young's moduli and the elastic shear moduli for unit and mortar. $h_m$ is the actual thickness of mortar joint.

### 4.2. Plastic behaviour

In the present study a rate independent composite interface model, defined by hyperbolic function (Eq. (4)) has been proposed (see Fig. 3). The proposed model is a simple extension of the Mohr-Coulomb criteria with cut-off in tension and cap-off in compression, which result in the single surface yield criteria capable of representing pressure-dependent friction shear failure and cracking by cut-off in-tension and crushing by cap-off in compression under combined normal and tangential stresses. The model includes all the mechanisms of the masonry failure and also overcomes the problem of the singularity that occurs in multi-surfaces yield criteria.

$$F(\boldsymbol{\sigma}, \boldsymbol{q}) := -[(C - \sigma_{nn}\tan(\phi))]^2 f_c(\boldsymbol{\sigma}, \boldsymbol{q}) f_t(\boldsymbol{\sigma}, \boldsymbol{q}) + \sigma_{tt}^2 \tag{4}$$

$$f_c(\boldsymbol{\sigma}, \boldsymbol{q}) := \frac{2}{\pi}\arctan\left(\frac{\sigma_{nn} - \zeta}{\alpha_c}\right) \tag{5}$$

$$f_t(\boldsymbol{\sigma}, \boldsymbol{q}) := \frac{2}{\pi}\arctan\left(\frac{\xi - \sigma_{nn}}{\alpha_t}\right) \tag{6}$$

where the vector $\boldsymbol{q} = \boldsymbol{q}(C, C_q, \phi, \psi, \xi, \zeta)$ is a function of six internal hardening parameters, which implicate the apparent cohesion $(C, C_Q)$, friction angle $(\phi)$, dilation angle $(\psi)$, tension strength $(\xi)$ and compression strength $(\zeta)$. In the yield function, $\xi$ denotes tension cut-off and $\zeta$ denotes compression cap. The function $f_c(\boldsymbol{\sigma}, \boldsymbol{q})$


**Fig. 1.** Simplified micro-modelling.

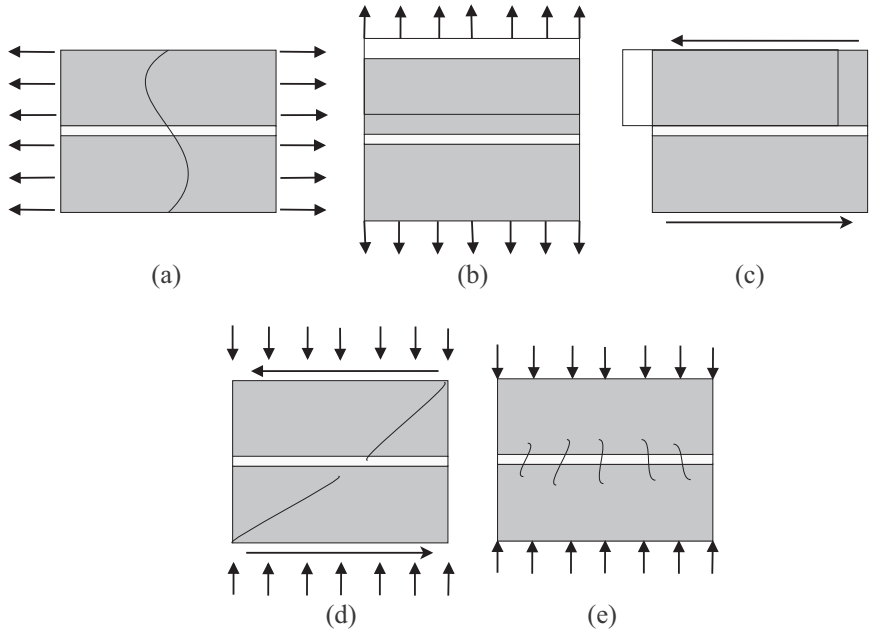


**Fig. 2.** Prominent masonry failure mechanisms: (a) unit direct tensile cracking; (b) joint tensile cracking; (c) joint slipping; (d) unit diagonal tensile cracking; (e) masonry crushing.

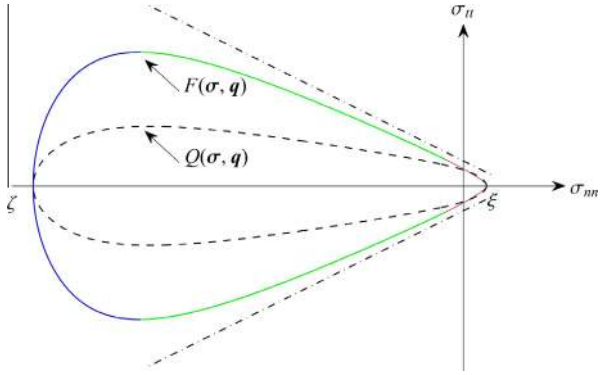


**Fig. 3.** Trace of yield function $F(\boldsymbol{\sigma},\boldsymbol{q})$ and potential function $Q(\boldsymbol{\sigma},\boldsymbol{q})$; red, green, blue lines represents the tension-cut, shear and compression-cap region respectively. (For interpretation of the references to colour in this figure legend, the reader is referred to the web version of this article.)

and $f_t(\boldsymbol{\sigma},\boldsymbol{q})$ are the compression cap and tension cut-off functions respectively. The function $f_c(\boldsymbol{\sigma},\boldsymbol{q})$ has the zero value at the cap and the function $f_t(\boldsymbol{\sigma},\boldsymbol{q})$ has zero value at tension-cut. For all other stress-states both the function have value approximately equal to one. The parameters $\alpha_c$ and $\alpha_t$ control the curvature of the compression cap and tension cut-off at transition region.

A non-associated formulation is used because friction and dilatancy angles are considerably different [82,83]. Therefore, the plastic potential is described in terms of another hyperbolic function with different values of apparent cohesion ($C_Q$) and frictional angle (dilation angle ($\psi$)), with same tensile ($\xi$) and compressive strength ($\zeta$). The expression of potential function reads

$$Q(\boldsymbol{\sigma},\boldsymbol{q}) := -[C_Q - \sigma_{nn}\tan(\psi)]^2 f_c(\boldsymbol{\sigma},\boldsymbol{q}) f_t(\boldsymbol{\sigma},\boldsymbol{q}) + \sigma_{tt}^2 \tag{7}$$

### 4.3. Evolution laws

Evolution laws for hardening or softening behaviour for the composite interface model is defined by the rate of plastic work per unit of volume. During plastic loading internal variables can be express as

$$\dot{\boldsymbol{W}}^p := \boldsymbol{\sigma}^T \dot{\boldsymbol{\epsilon}}^p \tag{8}$$

where $\dot{\boldsymbol{W}}^p$ is the rate of plastic work hardening per unit of volume. In the present study, evolution of yield surface in tension-shear and compression-shear region has been assumed such that during plastic loading in tension-shear region, tensile strength ($\xi$) decreases exponentially while friction angle ($\phi$) remain unchanged, and in compression-shear region both friction and tensile strength both degrades exponentially. In addition, the compression strength changes when plastic loading path intersects with the compression cap. The above assumptions can be expressed by four internal variables i.e. $\dot{\boldsymbol{W}}^p : \dot{\boldsymbol{W}}^p(\dot{w}_1^p, \dot{w}_2^p, \dot{w}_3^p, \dot{w}_4^p)$ where $\dot{w}_1^p$ and $\dot{w}_2^p$ represent degradation in tensile strength, $\dot{w}_2^p$ and $\dot{w}_3^p$ govern the frictional strength degradation and $\dot{w}_4^p$ gives change in the compression strength.

$$\dot{w}_1^p := \langle\sigma_{nn}\rangle \dot{u}_{nn}^p \tag{9}$$

$$\dot{w}_2^p := (\sigma_{tt} - \sigma_{tt_{r1}} sign(\sigma_{tt}))\dot{u}_{tt}^p \tag{10}$$

$$\dot{w}_3^p := (\sigma_{tt_{r1}} - \sigma_{tt_{r2}}) sign(\sigma_{tt}) \dot{u}_{tt}^p \tag{11}$$

$$\dot{w}_4^p := \langle\langle\sigma_{nn}\rangle\rangle \dot{u}_{nn}^p \quad for\ \sigma_{nn} < \zeta_c \tag{12}$$

where the symbol $\langle\rangle$ denotes for Macaulay bracket and $\langle x\rangle = (x + |x|)/2$ and $\langle\langle x\rangle\rangle = (x - |x|)/2$. $\zeta_c$ denotes the transient point from compression cap to Mohr-Coulomb friction envelope. $\sigma_{tt_{r1}}$ is the tangential strength when tensile strength is completely exhausted; $\sigma_{tt_{r2}}$ is minimum tangential strength for the final contracted yield surface. In tension-shear region, $\sigma_{tt_{r1}}$ and $\sigma_{tt_{r2}}$ are assumed to be zero and in compression-shear region they can be express as

$$\sigma_{tt_{r1}}^2 = -2C_r \tan\phi\, f_c f_t \tag{13}$$

$$\sigma_{tt_{r2}}^2 = -2C_r \tan\psi_r\, f_c f_t \tag{14}$$

In tension-shear region, during plastic loading the yield surface will contract until the tensile strength is exhausted and cohesion reaches a minimum value see Fig. 4(a) i.e. yield surface contracts from $F_0$ to $F_1$. While in compression-shear region, plastic loading reduces the tensile strength, cohesion as well as friction angle to its residual value (i.e. yield surface contracts to $F_2$). If the plastic loading path intersects the compression cap region, yield surface will evolve due to hardening in compression see Fig. 4(b) i.e. yield

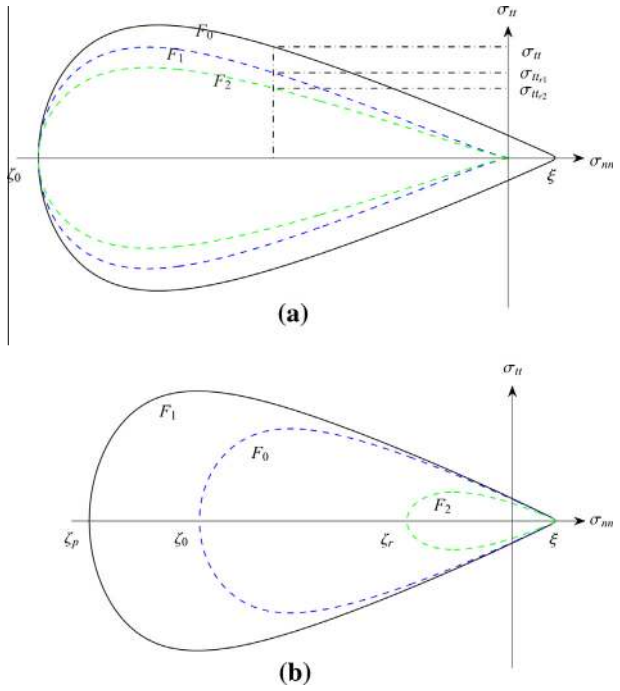


**Fig. 4.** Evolution of yield surfaces: (a) tension shear region; (b) compression region.

surface evolves from $F_0$ to $F_1$. After the compression-strength reaches its maximum value, there is a subsequent softening and compression strength reduces to minimum value due to contraction of yield surface i.e. yield surface contracts from $F_1$ to $F_2$.

The hardening parameter $\boldsymbol{q}$ can be related to the internal variables as follows

$$C := C_r + (C_0 - C_r)\exp^{-\beta_C\left(\frac{w_1^p}{G_f^I} + \frac{w_2^p}{G_f^{II}}\right)} \tag{15}$$

$$C_Q := C_{Q_r} + (C_{Q_0} - C_{Q_r})\exp^{-\beta_{C_Q}\left(\frac{w_1^p}{G_f^I} + \frac{w_2^p}{G_f^{II}}\right)} \tag{16}$$

$$\phi := \phi_r + (\phi_0 - \phi_r)\exp^{-\beta_\phi w_3^p} \tag{17}$$

$$\psi := \psi_r + (\psi_0 - \psi_r)\exp^{-\beta_\psi w_3^p} \tag{18}$$

$$\xi := \xi_0 \exp^{-\beta_\xi\left(\frac{w_1^p}{G_f^I} + \frac{w_2^p}{G_f^{II}}\right)} \tag{19}$$

$$\zeta = \begin{cases} \zeta_0 + (\zeta_p - \zeta_0)\sqrt{\left(\frac{2w_4^p}{w_p}\right) - \left(\frac{w_4^p}{w_p}\right)^2} & \text{if} \quad w_4^p \leqslant w_p \\ \zeta_0 + (\zeta_p - \zeta_p)\left(\frac{w_4^p - w_p}{w_m - w_p}\right)^2 & \text{if} \quad w_p \leqslant w_4^p \leqslant w_m \\ \zeta_r + (\zeta_m - \zeta_r)\exp^{\beta_\zeta\left(\frac{w_4^p - w_p}{\zeta_m - \zeta_r}\right)} & \text{if} \quad w_4^p > w_m \end{cases} \tag{20}$$

where $G_f^I$ and $G_f^{II}$ are the mode *I* and mode *II* fracture energy and $\beta_i$ is a parameter that controls the softening of the internal variable. The subscript 0 stands for initial value and *r* for residual value whereas subscript *p* and *m* indicate intermediate values. The preceding hardening equation can be written in a compact form as follows

$$\dot{\boldsymbol{W}}^p = \boldsymbol{H}\dot{\boldsymbol{\epsilon}}^p \tag{21}$$

### 4.4. Elastic–plastic tangent modulus

The total strain can be decomposed into sum of elastic strain and plastic strain i.e.

$$\boldsymbol{\epsilon} = \boldsymbol{\epsilon}^e + \boldsymbol{\epsilon}^p \tag{22}$$

where $\boldsymbol{\epsilon}^e$ and $\boldsymbol{\epsilon}^p$ are the elastic strain and plastic strain or irreversible strain respectively and the notion of irreversibility of plastic flow can be introduced by non-associated flow rule. It can be written in rate form as

$$\dot{\boldsymbol{\epsilon}}^p = \dot{\lambda}\boldsymbol{m} \tag{23}$$

where $\dot{\lambda}$ is the constant slip rate or plastic multiplier. The plastic multiplier can be found by checking the consistency condition (persistency condition) together with Kuhn-Tucker condition ($F \leq 0, \dot{\lambda} \geqslant 0, \dot{\lambda}F = 0$). The consistency condition can be written as $\dot{\lambda}\dot{F} = 0$ for yield condition $\dot{\lambda} > 0$ and $\dot{F} = 0$ and we can be written it as

$$\dot{F} = \frac{\partial F}{\partial \boldsymbol{\sigma}}\dot{\boldsymbol{\sigma}} + \frac{\partial F}{\partial \boldsymbol{q}}\dot{\boldsymbol{q}} = 0 \tag{24}$$

$$\dot{\lambda} = \frac{\boldsymbol{nK}\boldsymbol{\epsilon}}{\boldsymbol{n}^T\boldsymbol{K}\boldsymbol{m} + \boldsymbol{p}^T\boldsymbol{\varpi}} \tag{25}$$

In which $\boldsymbol{m} := \partial Q/\partial\boldsymbol{\sigma}$, $\boldsymbol{n} := \partial F/\partial\boldsymbol{\sigma}$, $\boldsymbol{p} := \partial Q/\partial\lambda, \boldsymbol{\varpi} := (\partial\boldsymbol{q}/\partial\boldsymbol{W}^p)(\partial\boldsymbol{W}^p/\partial\boldsymbol{\epsilon}^p)(\partial\boldsymbol{\epsilon}^p/\partial\lambda) = (\partial\boldsymbol{q}/\partial\boldsymbol{W}^p)\boldsymbol{Hm}$. Now we can define hardening parameter in its rate form as $\boldsymbol{q} = \dot{\lambda}\boldsymbol{\varpi}$. Putting the plastic multiplier ($\dot{\lambda}$) in the rate form of stress-strain relationship to get elasto-plastic tangent modulus $\boldsymbol{K}^{ep}$, i.e.

$$\dot{\boldsymbol{\sigma}} = \boldsymbol{K}(\dot{\epsilon} - \dot{\lambda}\boldsymbol{m}) = \boldsymbol{K}^{ep}\dot{\epsilon} \tag{26}$$

$$\boldsymbol{K}^{ep} = \boldsymbol{K} - \frac{\boldsymbol{Km} \otimes \boldsymbol{nK}}{\boldsymbol{n}^T\boldsymbol{K}\boldsymbol{m} + \boldsymbol{p}^T\boldsymbol{\varpi}} \tag{27}$$

### 4.5. Algorithmic aspect of local and global solver

In the present section, the composite interface model is implemented into a finite element framework with elastic-plastic continuum elements, which gives rise to a set of non-linear algebraic-differential equations, and are to be solved. The Newton–Raphson scheme is used to solve non-linear system of equations, which leads to combined local and global approach. Local solver provides the new internal state variable for a given relative displacement, subsequently global solver provides the solution for the unbalanced force to accommodate stress distribution within the finite load increments. In this section, numerical strategy is presented at both local (Constitutive level) and global level (Structural level).

#### 4.5.1. Elastic predictor–plastic corrector strategy

The implicit backward Euler integration method is used to integrate the differential constitutive equations. The backward Euler method is a first order (i.e. local truncation error is $O(h^2)$ for a single step) method and is unconditionally stable. The integration procedure leads to a set of algebraic-incremental equations, which can be split in to elastic predictor, followed by plastic corrector if and only if the trial stress-state violates the current yield condition.

The time discretization of an interval of interest as $[0,\ T] = \bigcup_{n=1}^{N}[t_n, t_{n+1}]$. The relevant problem can be seen with in time interval $[t_n, t_{n+1}]$. It is assumed that the stress-state $(\boldsymbol{\sigma}_n, \boldsymbol{q}_n)$ at current time $t = t_n$ should satisfy the equilibrium conditions and be admissible. For prescribed increment in strain $\dot{\boldsymbol{\epsilon}}$, at the next time step $t_{n+1} = t_n + \Delta t$ the strain is given by $\boldsymbol{\epsilon}_{n+1} = \boldsymbol{\epsilon}_n + \Delta\boldsymbol{\epsilon}$, and this can be split into two part i.e. $\Delta\boldsymbol{\epsilon} = \Delta\boldsymbol{\epsilon}^e + \Delta\boldsymbol{\epsilon}^p$. According to the elastic predictor-plastic correct strategy, the stress and internal variables can be written in their incremental form as

$$\boldsymbol{\sigma}_{n+1} = \boldsymbol{\sigma}_n + \boldsymbol{K}\Delta\boldsymbol{\epsilon}^e = \boldsymbol{\sigma}_n + \boldsymbol{K}(\Delta\boldsymbol{\epsilon} - \Delta\boldsymbol{\epsilon}^p) \tag{28}$$

$$\boldsymbol{\sigma}_{n+1} = \boldsymbol{\sigma}_{n+1}^{trial} + \Delta\lambda_{n+1}\boldsymbol{K}\boldsymbol{m}_{n+1} \tag{29}$$

$$\boldsymbol{q}_{n+1} = \boldsymbol{q}_n + \Delta\lambda_{n+1}\boldsymbol{\varpi}_{n+1} \tag{30}$$

where $\boldsymbol{\sigma}_{n+1}^{trial} = \boldsymbol{\sigma}_n + \boldsymbol{K}\Delta\boldsymbol{\epsilon}$ is the trial stress. During the elastic predictor step (say point A), if the trial stress goes outside the yield surfaces at the point B (see Fig. 5) after cutting the yield surface at the contact

point $o; F(\boldsymbol{\sigma}^{trial}_{n+1}, \boldsymbol{q}_{n+1}) > 0$, then plastic corrector step projects the stress-state at the point D after the evolution or contraction of the yield surface due to the change in internal variable. In the Fig. 5 point $C$ represents the final converged stress-state for an elastic-perfectly plastic model. In the present study plastic step mobilises the plastic work which changes the internal hardening parameter ($\boldsymbol{q}$) that expands or contracts the yield surface. It should be noted that the solution of the plastic corrector step must satisfy the full consistency at point $D$, rather than differential consistency ($\dot{F} = 0$).

$$F(\boldsymbol{\sigma}_{n+1}, \boldsymbol{q}_{n+1}) = 0 \tag{31}$$

*4.5.2. Contact point*

The plastic corrector step only produces the change in the stress and internal variable ($\boldsymbol{\sigma}_n, \boldsymbol{q}_n$). Therefore, it is very important to find the contact point for the present elastic predictor step. Mathematically, it can be express as

$$F(\boldsymbol{\sigma}_n + \gamma\Delta\boldsymbol{\sigma}, \boldsymbol{q}_n) = 0 \tag{32}$$

where $\boldsymbol{\sigma}_n, \boldsymbol{q}_n$ are the variables from the last converged elastic or plastic step, and $\gamma$ is unknown integer within the range [0 1], which converges the stress to the contact point.

*4.5.3. Local iteration strategy*

The backward Euler method gives rise to non-linear system of equations, which has to be solved to get actual stress state. In the present study full Newton–Raphson method is used to solve non-linear system of equations. It provides quadratic convergence with initial root sufficiently close, and also ensures the asymptotic quadratic convergence at the global level for structural equilibrium. Newton–Raphson strategy is used for the solution of non-linear equation in monolithic format, as illustrated in the [84–86] for the J2 plasticity. The strategy is highly influenced by the choice of the independent variables and sequence of the numerical operations. It requires the determination of residual for the set non-linear Eqs. (29)–(31). It can be written as

$$\boldsymbol{r}(\boldsymbol{\sigma}_{n+1}, \boldsymbol{q}_{n+1}, \Delta\lambda_{n+1}) = \begin{cases} \boldsymbol{\sigma}_{n+1} - \boldsymbol{\sigma}^{trial}_{n+1} + \Delta\lambda_{n+1}\boldsymbol{K}\boldsymbol{m}_{n+1} = 0 \\ \boldsymbol{q}_{n+1} - \boldsymbol{q}_n + \Delta\lambda_{n+1}\varpi_{n+1} = 0 \\ F(\boldsymbol{\sigma}_{n+1}, \boldsymbol{q}_{n+1}) = 0 \end{cases} \tag{33}$$

Linearization of the residual, and expanding the residual. we can write

$$\boldsymbol{r}(\boldsymbol{\sigma} + \delta\boldsymbol{\sigma}, \boldsymbol{q} + \delta\boldsymbol{q}, \Delta\lambda + \delta\lambda) = \boldsymbol{r}(\boldsymbol{\sigma}, \boldsymbol{q}, \Delta\lambda) + \frac{\boldsymbol{r}(\boldsymbol{\sigma}, \boldsymbol{q}, \Delta\lambda)}{\partial(\boldsymbol{\sigma}, \boldsymbol{q}, \lambda)} \begin{bmatrix} \delta\boldsymbol{\sigma} \\ \delta\boldsymbol{q} \\ \delta\lambda \end{bmatrix} + O(\delta^2) \tag{34}$$

where the truncation after first order term is zero ($O(\delta^2) \cong 0$) and $\frac{\boldsymbol{r}(\boldsymbol{\sigma}, \boldsymbol{q}, \Delta\lambda)}{\partial(\boldsymbol{\sigma}, \boldsymbol{q}, \lambda)}$ is the gradient of residual with respect to its dependent variable i.e. $\boldsymbol{\sigma}, \boldsymbol{q}, \lambda$ commonly known as Jacobian. The Jacobian for residual at time step $n+1$ can be express as

$$\boldsymbol{J}(\boldsymbol{\sigma}_{n+1}, \boldsymbol{q}_{n+1}, \Delta\lambda_{n+1}) = \begin{bmatrix} \boldsymbol{I} + \Delta\lambda\boldsymbol{K}\frac{\partial \boldsymbol{m}}{\partial \boldsymbol{\sigma}} & \Delta\lambda\boldsymbol{K}\frac{\partial \boldsymbol{m}}{\partial \boldsymbol{q}} & \boldsymbol{K}\boldsymbol{m} \\ -\Delta\lambda\boldsymbol{K}\frac{\partial \varpi}{\partial \boldsymbol{\sigma}} & -\Delta\lambda\boldsymbol{K}\frac{\partial \varpi}{\partial \boldsymbol{q}} & -\varpi \\ \frac{\partial \boldsymbol{F}}{\partial \boldsymbol{\sigma}} & \frac{\partial \boldsymbol{F}}{\partial \boldsymbol{q}} & 0 \end{bmatrix} \tag{35}$$

The actual solution is achieved by letting the residual go to zero for that current time step during plastic loading. This can be achieved by performing iterations cycles. The iteration will end when residual will become smaller then prescribed tolerance value.

$$0 = \boldsymbol{r}(\boldsymbol{\sigma}^k_{n+1}, \boldsymbol{q}^k_{n+1}, \Delta\lambda^k_{n+1}) + \boldsymbol{J}^{-1}(\boldsymbol{\sigma}^k_{n+1}, \boldsymbol{q}^k_{n+1}, \Delta\lambda^k_{n+1}) \begin{bmatrix} \delta\boldsymbol{\sigma}^{k+1}_{n+1} \\ \delta\boldsymbol{q}^{k+1}_{n+1} \\ \delta\lambda^{k+1}_{n+1} \end{bmatrix} \tag{36}$$

$$\begin{bmatrix} \delta\boldsymbol{\sigma}^{k+1}_{n+1} \\ \delta\boldsymbol{q}^{k+1}_{n+1} \\ \delta\lambda^{k+1}_{n+1} \end{bmatrix} = -\boldsymbol{J}^{-1}(\boldsymbol{\sigma}^k_{n+1}, \boldsymbol{q}^k_{n+1}, \Delta\lambda^k_{n+1})\ \boldsymbol{r}(\boldsymbol{\sigma}^k_{n+1}, \boldsymbol{q}^k_{n+1}, \Delta\lambda^k_{n+1}) \tag{37}$$

$$\begin{bmatrix} \boldsymbol{\sigma}^{k+1}_{n+1} \\ \boldsymbol{q}^{k+1}_{n+1} \\ \lambda^{k+1}_{n+1} \end{bmatrix} = \begin{bmatrix} \boldsymbol{\sigma}^{k}_{n+1} \\ \boldsymbol{q}^{k}_{n+1} \\ \lambda^{k}_{n+1} \end{bmatrix} + \begin{bmatrix} \delta\boldsymbol{\sigma}^{k+1}_{n+1} \\ \delta\boldsymbol{q}^{k+1}_{n+1} \\ \delta\lambda^{k+1}_{n+1} \end{bmatrix} \tag{38}$$

For starting the iteration a sufficiently close initial solution is required, as the convergence of local iteration cycle depends up on the initial root. Thus initial solution is chosen to be the elastic solution at the contact point.

$$\boldsymbol{\sigma}^0_{n+1} = \boldsymbol{\sigma}^{trial}_{n+1} + (1-\gamma)\Delta\boldsymbol{\sigma}; \quad \boldsymbol{q}^0_{n+1} = \boldsymbol{q}_n; \quad \Delta\lambda^0_{n+1} = 0 \tag{39}$$

Note that the variable $\Delta\lambda^0_{n+1}$ is taken equal to zero at first iteration of every new load step, as plastic multiplier captures the plastic process incrementally. The initial hardening parameter values $\boldsymbol{q}^0_{n+1}$ are the last converge hardening parameter values.

*4.5.4. Global iteration strategy*

The converged solution form local iteration strategy can be used for the determination of consistent tangent operator $\frac{\Delta\boldsymbol{\sigma}}{\Delta\boldsymbol{\epsilon}}$ for the current time step. Thus, in order to compute the tangent operator using the Jacobian, we have to differentiate the residual with respect to the strain and then using the chain rule we will get

$$\frac{\partial}{\partial\boldsymbol{\epsilon}} \begin{bmatrix} \boldsymbol{\sigma}_{n+1} - \boldsymbol{\sigma}^{trial}_{n+1} + \Delta\lambda_{n+1}\boldsymbol{K}\boldsymbol{m}_{n+1} \\ \boldsymbol{q}_{n+1} - \boldsymbol{q}_n + \Delta\lambda_{n+1}\varpi_{n+1} \\ F(\boldsymbol{\sigma}_{n+1}, \boldsymbol{q}_{n+1}) \end{bmatrix} = 0 \tag{40}$$

$$\frac{\partial}{\partial\boldsymbol{\epsilon}} \begin{bmatrix} \boldsymbol{\sigma} + \Delta\lambda\boldsymbol{K}\boldsymbol{m} \\ \boldsymbol{q} - \Delta\lambda\varpi \\ F(\boldsymbol{\sigma}, \boldsymbol{q}) \end{bmatrix}_{n+1} = \frac{\partial}{\partial\boldsymbol{\epsilon}} \begin{bmatrix} \boldsymbol{\sigma} + \boldsymbol{K}\Delta\boldsymbol{\epsilon} \\ \boldsymbol{q} \\ 0 \end{bmatrix}_n \tag{41}$$

$$\begin{bmatrix} \frac{\partial}{\partial\boldsymbol{\sigma}} & \frac{\partial}{\partial\boldsymbol{q}} & \frac{\partial}{\partial\lambda} \end{bmatrix}_{n+1} \begin{bmatrix} \boldsymbol{\sigma} + \Delta\lambda\boldsymbol{K}\boldsymbol{m} \\ \boldsymbol{q} - \Delta\lambda\varpi \\ F(\boldsymbol{\sigma}, \boldsymbol{q}) \end{bmatrix}_{n+1} \begin{bmatrix} \frac{\partial\boldsymbol{\sigma}}{\partial\boldsymbol{\epsilon}} & \frac{\partial\boldsymbol{q}}{\partial\boldsymbol{\epsilon}} & \frac{\partial\lambda}{\partial\boldsymbol{\epsilon}} \end{bmatrix}^T_{n+1} = \frac{\partial}{\partial\boldsymbol{\epsilon}} \begin{bmatrix} \boldsymbol{\sigma} + \boldsymbol{K}\Delta\boldsymbol{\epsilon} \\ \boldsymbol{q} \\ 0 \end{bmatrix}_n \tag{42}$$

$$\boldsymbol{J}(\boldsymbol{\sigma}_{n+1}, \boldsymbol{q}_{n+1}, \Delta\lambda_{n+1}) \cdot \begin{bmatrix} \frac{\partial\boldsymbol{\sigma}}{\partial\boldsymbol{\epsilon}} & \frac{\partial\boldsymbol{q}}{\partial\boldsymbol{\epsilon}} & \frac{\partial\lambda}{\partial\boldsymbol{\epsilon}} \end{bmatrix}^T_{n+1} = \begin{bmatrix} \boldsymbol{K} \\ 0 \\ 0 \end{bmatrix} \tag{43}$$

$$\begin{bmatrix} \left[\frac{\partial\boldsymbol{\sigma}}{\partial\boldsymbol{\epsilon}}\right]_{2x2} \\ \left[\frac{\partial\boldsymbol{q}}{\partial\boldsymbol{\epsilon}}\right]_{6x2} \\ \left[\frac{\partial\lambda}{\partial\boldsymbol{\epsilon}}\right]_{1x2} \end{bmatrix}_{9x2} = \boldsymbol{J}^{-1}(\boldsymbol{\sigma}_{n+1}, \boldsymbol{q}_{n+1}, \Delta\lambda_{n+1})_{9x9} \begin{bmatrix} \boldsymbol{K} \\ 0 \\ 0 \end{bmatrix}_{9x2} \tag{44}$$

The consistent tangent operator can extracted from the preceding expression, and we can defined the consistent tangent operator as:

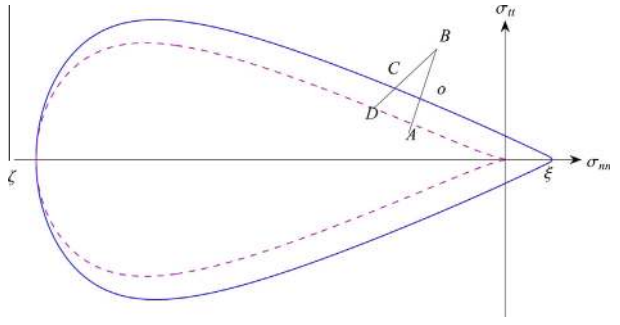


**Fig. 5.** Plot of the integration process, initial converged stress at point $A(\boldsymbol{\sigma}_n)$, contact point at $o(\boldsymbol{\sigma}^0_{n+1})$, trial stress $B(\boldsymbol{\sigma}^{trial}_{n+1})$, final stress for elastic-perfectly plastic model at point $C$, final converged stress for evolved or shrunk yield surface at point $D(\boldsymbol{\sigma}_{n+1})$.

$$\left[\frac{\partial\boldsymbol{\sigma}}{\partial\boldsymbol{\epsilon}}\right]_{2x2} = O_{2x2}\left\{\boldsymbol{J}^{-1}(\boldsymbol{\sigma}_{n+1},\boldsymbol{q}_{n+1},\Delta\lambda_{n+1})_{9x9}\begin{bmatrix}\boldsymbol{K}\\0\\0\end{bmatrix}_{9x2}\right\} \tag{45}$$

### 4.6. Algorithmic implementation

The plasticity based composite interface model is implemented in commercial finite element software ABAQUS [87] by writing the user defined subroutine UMAT, which allows to define a user defined mechanical constitutive model for a material. During the analysis, the UMAT is called at the all integration points of the elements. At end of the increment UMAT updates the stress, internal state variables and elasto-plastic tangent operator. The proposed numerical integration algorithm implemented in the UMAT is presented in Algorithm 1.

**Algorithm 1.** Monolithic numerical integration algorithm

**Steps**

**1.** Recover Solution Dependent Variables from the last converged iteration cycle

$$\boldsymbol{\sigma}_{n+1},\boldsymbol{q}_n,\boldsymbol{W}_n^p,\boldsymbol{\epsilon}_n^p$$

**2.** Compute trial elastic stress

$$\boldsymbol{\sigma}_{n+1}^{trial} = \boldsymbol{\sigma}_n + \boldsymbol{K}\Delta\boldsymbol{\epsilon}$$

**3.** Compute the yield function $F^{trial}(\boldsymbol{\sigma}_{n+1}^{trial},\boldsymbol{q}_n)$

**4.** Check for the yield condition

**if** $F^{trial}(\boldsymbol{\sigma}_{n+1}^{trial},\boldsymbol{q}_n) < 0$ **then**

  **Elastic State**

  update $\boldsymbol{\sigma}_{n+1} = \boldsymbol{\sigma}_{n+1}^{trial}$;

  update $\boldsymbol{q}_{n+1} = \boldsymbol{q}_n$ ;

  update $\boldsymbol{W}_n^p = \boldsymbol{W}_n^p$ ;

  update $\boldsymbol{\epsilon}_n^p = \boldsymbol{\epsilon}_n^p$ ;

**else**

  **Plastic State**

  Compute the contact point $F(\boldsymbol{\sigma}_n + \gamma\Delta\boldsymbol{\sigma},\boldsymbol{q}_n)$;

  **while** $\|\boldsymbol{r}(\boldsymbol{\sigma}_n,\boldsymbol{q}_n,\Delta\lambda_n)\| < tol$ **do**

    Compute $\boldsymbol{n}_n^k,\boldsymbol{m}_n^k,\boldsymbol{\varpi}_n^k$;

    Compute $\boldsymbol{J}_n^k(\boldsymbol{\sigma}_n^k,\boldsymbol{q}_n^k,\Delta\lambda_n^k) = \dfrac{\boldsymbol{r}(\boldsymbol{\sigma}_n^k,\boldsymbol{q}_n^k,\Delta\lambda_n^k)}{\partial(\boldsymbol{\sigma}_n^k,\boldsymbol{q}_n^k,\lambda_n^k)}$;

    Compute $\delta(\boldsymbol{\sigma}_n,\boldsymbol{q}_n,\lambda_n)^{k+1} = -\boldsymbol{J}^{-1}(\boldsymbol{\sigma}_n^k,\boldsymbol{q}_n^k,\Delta\lambda_n^k)\boldsymbol{r}(\boldsymbol{\sigma}_n^k,\boldsymbol{q}_n^k,\Delta\lambda_n^k)$;

    Compute $[\boldsymbol{\sigma}_n,\boldsymbol{q}_n,\lambda_n]^{k+1} = [\boldsymbol{\sigma}_n,\boldsymbol{q}_n,\lambda_n]^k + \delta(\boldsymbol{\sigma}_n,\boldsymbol{q}_n,\lambda_n)^{k+1}$;

  **end**

  update $\boldsymbol{\sigma}_{n+1} = \boldsymbol{\sigma}_n^{k+1}$;

  update $\boldsymbol{q}_{n+1} = \boldsymbol{q}_n^{k+1}$;

  update $\boldsymbol{W}_{n+1}^p = (\boldsymbol{W}_n^p)^{k+1}$ ;

  update $\boldsymbol{\epsilon}_n^p = (\boldsymbol{\epsilon}_n^p)^{k+1}$ ;

  Compute $\boldsymbol{K}^{ep}$

**end**

### 4.7. Verification examples

In order to verify the proposed composite interface model various verification examples have been considered in this section. The formulated constitutive model is verified by implementing a single zero-thickness interface, which is a 4-node two dimensional cohesive element with two integration point. The material parameter used for verification are tabulated in Tables 1 and 2 obtained from the calibration process. Specifically, to find the values of mode I and mode II fracture energy, it is assumed that $G_f^I = 5G_{f,min}^I$ and $G_f^{II} = 10G_f^I$, where $G_{f,min}^I = \xi_0^2/2k_{nn}$ corresponding to the perfectly brittle tensile fracture. The verification examples include interface in tension, compression and shear mode condition. The implementation is done in ABAQUS, by using the user defined subroutine (UMAT).

#### 4.7.1. Direct tension test

In this test the interface is subjected to direct tension. A normal relative displacement is applied to the nodes on the top face of the interface element while all the degrees of freedom on the bottom face are fixed. Fig. 6 shows the variation of tensile strength $\xi$ with mix mode fracture energy $\frac{w_1^p}{G_f^I}+\frac{w_2^p}{G_f^{II}}$. The response exhibits a exponential degradation of the tensile strength and matches well with the analytical values.

#### 4.7.2. Direct compression test

In this test the interface is subjected to direct compression. The test is performed to check the functionality of the compression cap. A normal relative displacement is applied to produce the pure compression state in the interface and variation of compression strength ($\zeta$) with work hardening parameter $w_4^p$ is traced and compared with the analytical values by solving Eq. (20) It can be observed from Fig. 7, that the internal hardening variable ($\zeta$) coincides well with the analytical values.

#### 4.7.3. Direct shear test under compressive stress

In this test the interface is subjected to direct shear test under different normal compressive stress. The interface element is loaded with normal compressive stress. Then, a relative shear displacement is applied at the top surface, while all degrees of freedom on the bottom face are kept fixed. This load sequence is repeated for various levels of constant normal compressive stress. The results of this test are shown in Fig. 8(a). A plot of distribution of tangential stress with relative tangential displacement are plotted for different compressive stress (0.1, 1, 10 Mpa). A shear softening behaviour is observed. The result shows that the shear capacity of the interface increases with increase in compressive stress. After the initial elastic response, all response curves show a similar post-peak behaviour, with a steeper part given by the decrease of all softening parameters ($\boldsymbol{q}$). After that, $\xi$ remains zero, and the shear traction diminishes. Finally, all softening curves tend to the residual shear value that corresponds to the residual cohesion ($C_r$) and friction angle ($\phi_r$).

In Fig. 8(b), the distribution of normal displacements with relative tangential displacements is plotted. It can be observed that the dilatancy decreases with increase in compressive stress, and approaches a limiting value when the interface degrades to the residual dilation angle ($\psi_r$).

### 4.8. Sub stepping

The algorithm requires sub-stepping not only to ensure convergence of the solution but also to ensure the accuracy of the final solution at both local and global level. Fortunately it is possible to integrate the constitutive equations by sub-dividing the load at the constitutive level [88–90]. Based on these considerations, an adaptive sub-stepping scheme has been developed for the present composite interface model. This technique starts with the previous system of Eq. (33). The algebraic problem is modified significantly in order to obtain consistent tangent operator in the case of sub-stepping. It is assumed that any increment can be subdivided into $N$ sub-increments, which could be of different sizes but the sum of all sub-increments always equals to the total displacement at the end of the increment

$$\Delta\epsilon = \sum_{i=0}^{N}\Delta\epsilon^i = \Delta\epsilon(\eta^i) \tag{46}$$

**Table 1**
Elastic material property for the brick and joints.

| Brick | | Joint | |
|---|---|---|---|
| $E$ (N/mm$^2$) | $v$ | $k_{nn}$ (N/mm$^3$) | $k_{tt}$ (N/mm$^3$) |
| 16,700 | 0.15 | 82; 110; 82 | 36; 50; 36 |

**Table 2**
Inelastic material property for the joints.

| Tension | | Shear | | | | | Cap |
|---|---|---|---|---|---|---|---|
| $\xi_0$ (N/mm$^2$) | $G_f^I$ (Nmm/mm$^2$) | $C_0 \backslash C_r$ (N/mm$^2$) | $C_{Q0} \backslash C_{Qr}$ (N/mm$^2$) | $\phi_0 \backslash \phi_r$ (radian) | $\psi$ (radian) | $G_f^{II}$ (Nmm/mm$^2$) | $\zeta_p$ (N/mm$^2$) |
| 2 | $5\xi_0^2/2k_{nn}$ | $1.4\xi_0 \backslash 0.1C_0$ | $1.1\xi_0 \backslash 0.1C_{Q0}$ | 0.65\0.50 | 0.078 | $10G_f^I$ | 30 |

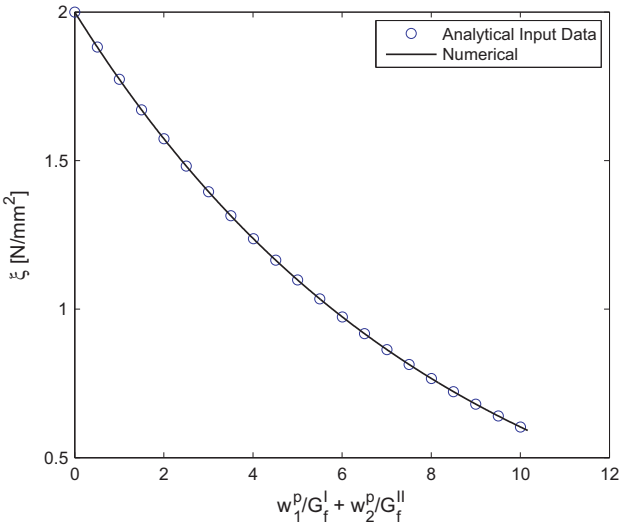


**Fig. 6.** Plot of distribution of tensile strength $\xi$ with $\left(\frac{w_1^p}{G_f^I} + \frac{w_2^p}{G_f^{II}}\right)$.

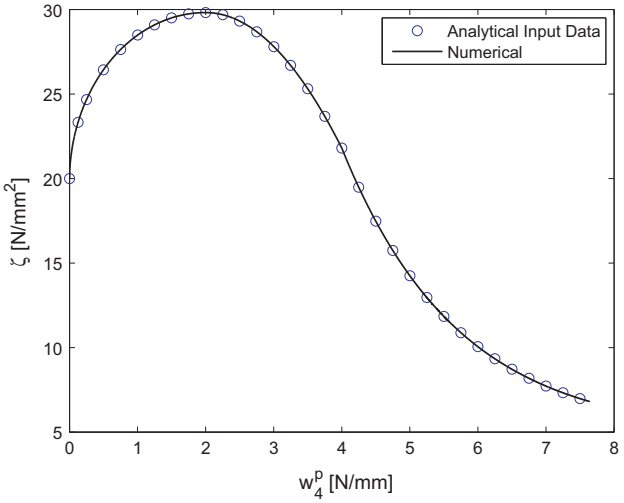


**Fig. 7.** Plot of distribution of compression strength $\zeta$ with $w_4^p$.

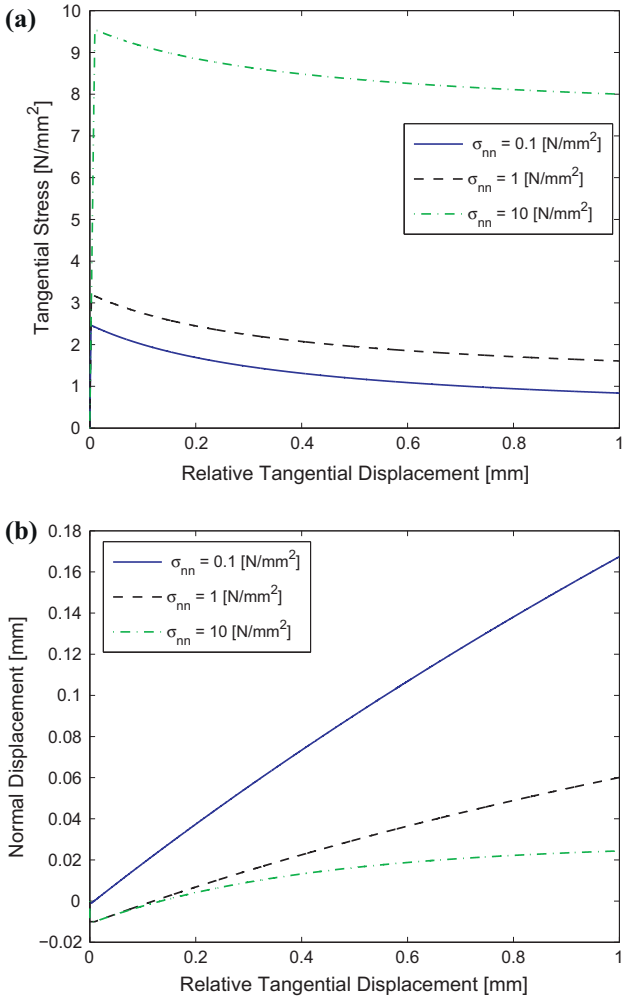


**Fig. 8.** Plot for direct shear test under different constant compressive stress: (a) distribution of tangential stress with relative tangential displacement; (b) distribution of normal displacements with relative tangential displacements.

where $0 < \eta^i < 1$ and $\sum_{i=0}^{N} \eta^i = 1$

Hence rewriting the Eq. (33), for sub-increment

$$\boldsymbol{r}(\boldsymbol{\sigma}^i, \boldsymbol{q}^i, \Delta\lambda^i) = \begin{cases} \boldsymbol{\sigma}^i - (\boldsymbol{\sigma}^{trial})^i + \Delta\lambda^i \boldsymbol{K}\boldsymbol{m}^i = 0 \\ \boldsymbol{q}^i - \boldsymbol{q}^{i-1} + \Delta\lambda^i \boldsymbol{\varpi}^i = 0 \\ F(\boldsymbol{\sigma}^i, \boldsymbol{q}^i) = 0 \end{cases} \tag{47}$$

Note that, now the independent variable of the system of equation are $\boldsymbol{\sigma}^i, \boldsymbol{q}^i, \Delta\lambda^i$ and the methodology for solving the equation is same as the one in previous section. For consistent tangent operator, taking the derivative of the equation with respect to $\Delta\epsilon$ and then apply the chain rule

$$\begin{bmatrix} \left[\frac{\partial \boldsymbol{\sigma}^i}{\partial \epsilon^i}\right]_{2x2} \\ \left[\frac{\partial \boldsymbol{q}^i}{\partial \epsilon^i}\right]_{6x2} \\ \left[\frac{\partial \lambda^i}{\partial \epsilon^i}\right]_{1x2} \end{bmatrix}_{9x2} = \boldsymbol{J}^{-1}(\boldsymbol{\sigma}_{n+1}^i, \boldsymbol{q}_{n+1}^i, \Delta\lambda_{n+1}^i)_{9x9} \begin{bmatrix} \eta^i \boldsymbol{K} \\ 0 \\ 0 \end{bmatrix}_{9x2} \tag{48}$$

The consistent tangent operator of a sub-increment can extracted from the preceding expression. The consistent tangent operator of the load step is obtained by linear combination of all sub-increments and can be written as

$$\left[\frac{\partial \boldsymbol{\sigma}}{\partial \epsilon}\right] = \sum_{i=0}^{N} \left[\frac{\partial \boldsymbol{\sigma}^i}{\partial \boldsymbol{\epsilon}^i}\right] \tag{49}$$

**Algorithm 2.** Monolithic numerical integration algorithm with sub-stepping

**Steps**

**1.** Recover Solution Dependent Variables from the last converged iteration cycle

$$\boldsymbol{\sigma}_{n+1}, \boldsymbol{q}_n, \boldsymbol{W}_n^p, \boldsymbol{\epsilon}_n^p$$

**2.** Compute trial elastic stress

$$\boldsymbol{\sigma}_{n+1}^{trial} = \boldsymbol{\sigma}_n + \boldsymbol{K}\Delta\boldsymbol{\epsilon}$$

**3.** Compute the yield function $F^{trial}(\boldsymbol{\sigma}_{n+1}^{trial}, \boldsymbol{q}_n)$

**4.** Check for the yield condition

**if** $F^{trial}(\boldsymbol{\sigma}_{n+1}^{trial}, \boldsymbol{q}_n) < 0$ **then**

  **Elastic State**

  update $\boldsymbol{\sigma}_{n+1} = \boldsymbol{\sigma}_{n+1}^{trial}$;

  update $\boldsymbol{q}_{n+1} = \boldsymbol{q}_n$ ;

  update $\boldsymbol{W}_n^p = \boldsymbol{W}_n^p$ ;

  update $\boldsymbol{\epsilon}_n^p = \boldsymbol{\epsilon}_n^p$ ;

**else**

  **Plastic State**

  Compute the contact point $F(\boldsymbol{\sigma}_n + \gamma\Delta\boldsymbol{\sigma}, \boldsymbol{q}_n)$;

  Compute $(\boldsymbol{K}^{ep})^0 = \gamma\boldsymbol{K}$ ;

  **while** $i < n$ **do**

    **while** $\|\boldsymbol{r}(\sigma_n, \boldsymbol{q}_n, \Delta\lambda_n)\| < tol$ **do**

      for simplicity superscript 'i' is not used ;

      Compute $\boldsymbol{n}_n^k, \boldsymbol{m}_n^k, \varpi_n^k$;

      Compute $\boldsymbol{J}_n^k(\boldsymbol{\sigma}_n^k, \boldsymbol{q}_n^k, \Delta\lambda_n^k) = \dfrac{\boldsymbol{r}(\boldsymbol{\sigma}_n^k, \boldsymbol{q}_n^k, \Delta\lambda_n^k)}{\partial(\boldsymbol{\sigma}_n^k, \boldsymbol{q}_n^k, \lambda_n^k)}$;

      Compute $\delta(\boldsymbol{\sigma}_n, \boldsymbol{q}_n, \lambda_n)^{k+1} = -\boldsymbol{J}^{-1}(\boldsymbol{\sigma}_n^k, \boldsymbol{q}_n^k, \Delta\lambda_n^k)\boldsymbol{r}(\boldsymbol{\sigma}_n^k, \boldsymbol{q}_n^k, \Delta\lambda_n^k)$;

      Compute $[\boldsymbol{\sigma}_n, \boldsymbol{q}_n, \lambda_n]^{k+1} = [\boldsymbol{\sigma}_n, \boldsymbol{q}_n, \lambda_n]^k + \delta(\boldsymbol{\sigma}_n, \boldsymbol{q}_n, \lambda_n)^{k+1}$;

    **end**

    update $(\boldsymbol{\sigma}_{n+1})^i = (\boldsymbol{\sigma}_n^{k+1})^i$;

    update $(\boldsymbol{q}_{n+1})^i = (\boldsymbol{q}_n^{k+1})^i$;

    update $(\boldsymbol{W}_{n+1}^p)^i = ((\boldsymbol{W}_n^p)^{k+1})^i$ ;

    Compute $(\boldsymbol{K}^{ep})^i$

  **end**

  update $\boldsymbol{\sigma}_{n+1} = (\boldsymbol{\sigma}_n^{k+1})^N$;

  update $\boldsymbol{q}_{n+1} = (\boldsymbol{q}_n^{k+1})^N$;

  update $\boldsymbol{W}_{n+1}^p = ((\boldsymbol{W}_n^p)^{k+1})^N$ ;

  Compute $\boldsymbol{K}^{ep} = \sum_{i=0}^{N} (\boldsymbol{K}^{ep})^i$

**end**

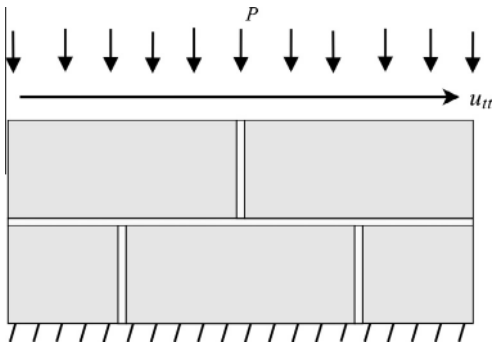


**Fig. 9.** Direct shear test set-up as per Atkinson et al. [83].

**Table 3**
Elastic material property for the brick and joints.

| Brick | | Joint | |
|---|---|---|---|
| $E$ (N/mm$^2$) | $\nu$ | $k_{nn}$ (N/mm$^3$) | $k_{tt}$ (N/mm$^3$) |
| 220 | 0.15 | 3.8 | 11.5 |

## 5. Validation example

### 5.1. Response of masonry bed joints in direct shear [83]

In this section, the capability of the proposed composite interface model is validated by comparing the finite element results with experimental results obtained by Atkinson et al. [83], in representing the shear behaviour of masonry mortar joints under different load conditions. In [83] the authors conducted direct shear tests using a servo-controlled loading apparatus to examine the response of brick masonry bed joints under monotonic and cyclic loadings, see Fig. 9. In each of these tests, first a uniformly distributed normal stress was applied ranging from 0.34 to 4.31 Mpa, and then four cycles of shear reversals were imposed under displacement control. The authors used old and new bricks with low- and high-strength mortars. In the present study, new bricks specimens with high-strength mortar has been considered for the validation, under three different levels of compressive stress (0.49, 1.34, 4.31 Mpa). The specimens consist of modern clay bricks [193 × 55 × 92 mm$^3$] and mortar joints [7 mm], prepared with a volumetric cement: lime : sand ratio (1:1.5:4.5). The bed joint area is equal to 92 × 398 mm$^2$ (0.037 m$^2$). The values of the material parameters used in the simulations are summarised in Tables 3 and 4. The stiffness of the brick is assumed to be 20 times the elastic normal stiffness of the mortar joint.

The comparison between numerical and experimental load-displacement curves is shown in Fig. 10, which shows that the proposed model is able to reproduce the shear behaviour of brick masonry bed joints not only in monotonic but also in cyclic loading. The experimental and numerical dilatancy curves show that, higher the compressive stress, smaller is the dilatancy and it is observed that the correlation of numerical and experimental results is good. The significant influence of dilatancy on the deformability and strength of an interface can be demonstrated by this numerical example. When the interface between the elastic region (elastic brick) is subjected to shear deformations under a normal confinement, Initially the normal stress on the interface is zero. However, since the elastic boundary prevents the interface from dilating freely, a significant compressive stress develops on the interface during the application of relative tangential displacement. Depending on the amount of dilatancy, controlled by the dilatancy parameter, the shear response can change from softening to hardening, and the shear strength of the interface can change by an order of magnitude.

### 5.2. Masonry shear wall (Vermeltfoort and Raijmakers)

A test was carried out on masonry shear wall by the author Vermeltfoort and Raijmakers [12,91]. The authors conducted the tests on two type of wall i.e. one without the opening and another with the opening. The authors used a set-up that consisted of a pier with a width to height ratio of one and with dimensions 990 × 1000 [mm$^2$]. It was built-up with 18 courses of which two courses were clamped in steel beam and only 16 courses were active. The wall was made up of wire cut solid clay [210 × 52 × 100 mm$^3$] and mortar [10 mm], prepared with a volumetric cement: lime: sand ratio (1:2:9). The test involves a

**Table 4**
Inelastic material property for the joints.

| Tension | | Shear | | | | | Cap |
|---|---|---|---|---|---|---|---|
| $\xi_0$ (N/mm$^2$) | $G_f^I$ (Nmm/mm$^2$) | $C_0 \backslash C_r$ (N/mm$^2$) | $C_{Q0} \backslash C_{Qr}$ (N/mm$^2$) | $\phi_0 \backslash \phi_r$ (radian) | $\psi_0 \backslash \psi_r$ (radian) | $G_f^{II}$ (Nmm/mm$^2$) | $\zeta_p$ (N/mm$^2$) |
| 0.65 | $5\xi_0^2/2k_{nn}$ | 1.2\0.12 | 1.2\0.12 | 0.67\0.57 | 0.35\0 | $10G_f^I$ | −16 |

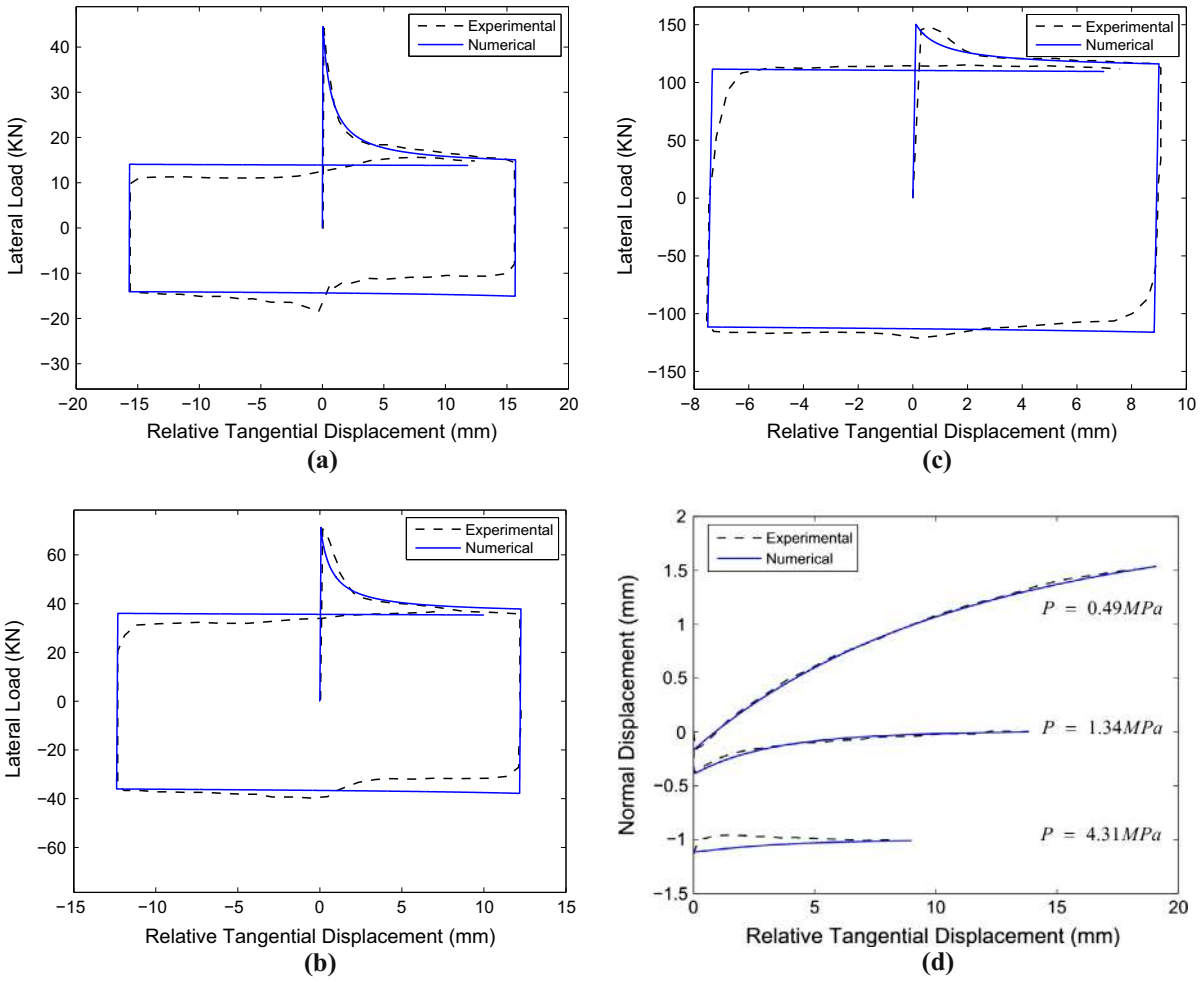


**Fig. 10.** Comparison between experimental results from direct shear test [83] and Numerical results obtained from the present model: (a) $P = 0.49$ MPa; (b) $P = 1.34$ MPa; (c) $P = 4.31$ MPa; (d) distribution of normal displacements with relative tangential displacements for different pressure.

**Table 5**
elastic material property for the brick and joints.

| Brick | | Joint | |
|---|---|---|---|
| $E$ (N/mm$^2$) | $v$ | $K_{nn}$ (N/mm$^3$) | $K_{tt}$ (N/mm$^3$) |
| 16,700 | 0.15 | 82; 110; 82 | 36; 50; 36 |

monotonically increasing horizontal load under different levels of uniformly distributed normal stress, keeping the bottom and top boundaries horizontally fixed. The material data is obtained from existing experimental results on tension, shear and compression from the sample collected for each wall. A four-noded bilinear plane stress quadrilateral, reduced integration, hourglass control (CPS4R) element with 4-degrees of freedom at each node were used to model the brick units, and four-noded two dimensional cohesive (COH2D4) element with two integration point were used to model the interface between the brick units. Total 2332 element

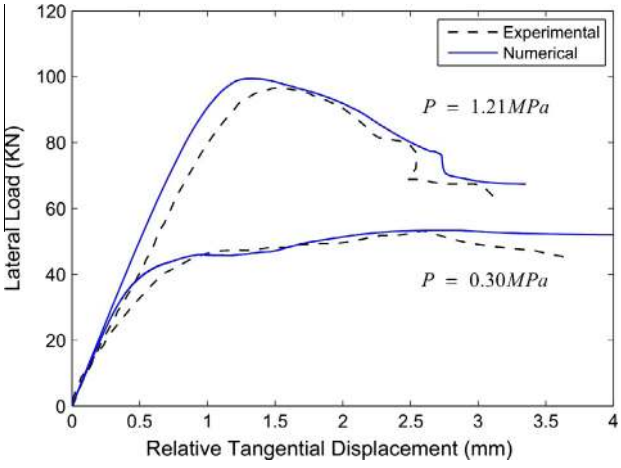


**Fig. 11.** Compression of experimental result and numerical result obtained from the proposed model.

**Table 6**
Inelastic material property for the joints.

| Tension | | Shear | | | | | Cap |
|---|---|---|---|---|---|---|---|
| $\xi_0$ (N/mm$^2$) | $G_f^I$ (Nmm/mm$^2$) | $C_0 \backslash C_r$ (N/mm$^2$) | $C_{Q0} \backslash C_{Qr}$ (N/mm$^2$) | $\phi_0 \backslash \phi_r$ (radian) | $\psi$ (radian) | $G_f^{II}$ (Nmm/mm$^2$) | $\zeta_p$ (N/mm$^2$) |
| 0.25; 0.16 | $5\frac{\xi_0^2}{2K_{nn}}$ | $1.4\xi_0 \backslash 0.1C_Q$ | $1.1\xi_0 \backslash 0.1C_Q$ | 0.65\0.50 | 0 | $10G_f^I$ | 11.5 |

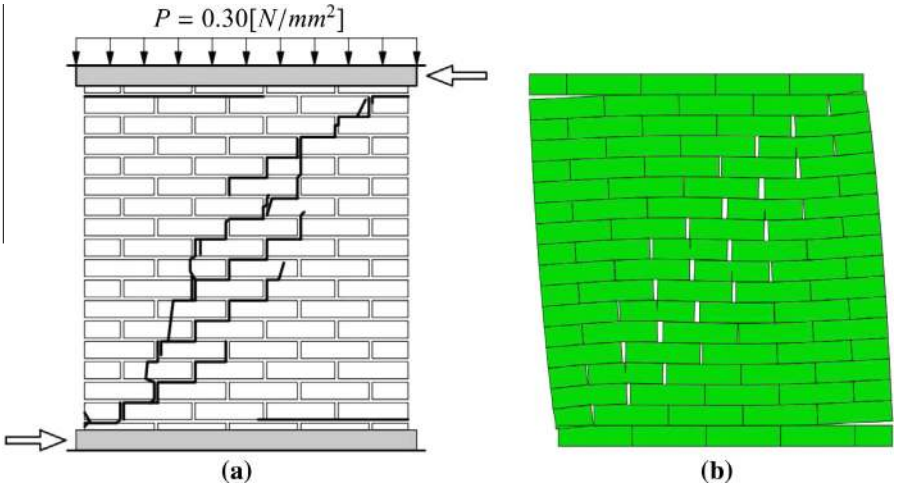


**Fig. 12.** Comparison of experimental and numerical failure patterns: (a) experimental patterns; (b) numerical patterns.

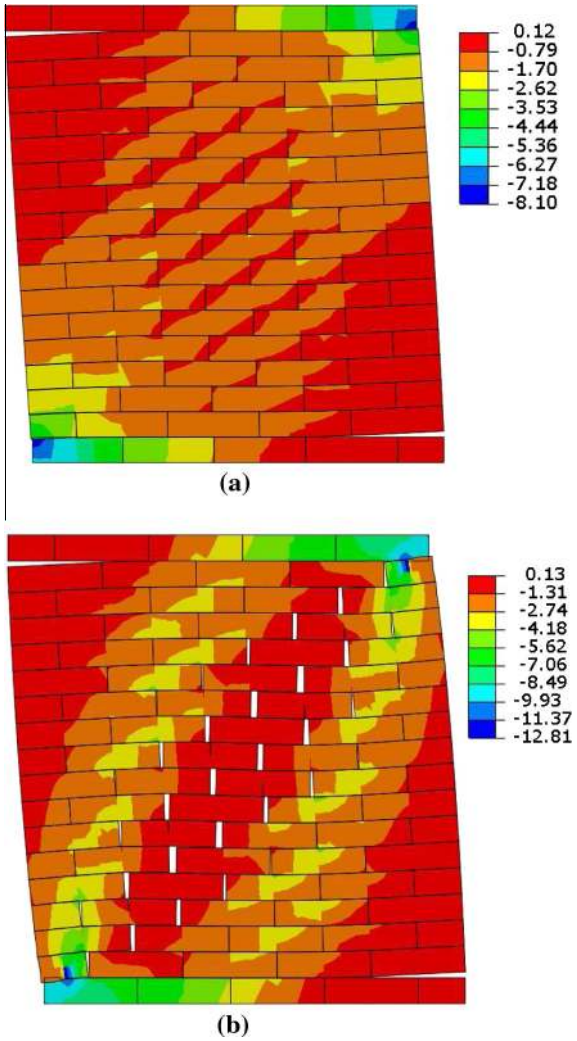


**Fig. 13.** plot for minimum principal stress (N/mm$^2$): (a) relative tangential displacement = 1.0 [mm]; (b) relative tangential displacement = 4.0 [mm].

were used in simulation for masonry shear wall by the author Vermeltfoort and Raijmakers.

The micro-properties of the shear wall material are obtained from [12,91] and are given in Tables 5 and 6. The hardening/softening law for the compression cap is defined by the set $\{\zeta, w_4^p\} = \{(\zeta_p/3, 0.0);\ (\zeta_p, 0.09);\ (\zeta_p/2, 0.49);\ (\zeta_p/7, \infty)\}$.

The comparison between numerical and experimental load-displacement curves are shown in Fig. 11. The experimental behaviour is satisfactorily reproduced by the proposed composite interface model. The crack pattern for the shear wall are presented in the Fig. 12. The non-linear behaviour of the shear wall is initiated by the horizontal tensile cracks, that develop at the bottom and top of the wall at an early loading stage, see Fig. 13(a). On further loading the tensile cracking is followed by a diagonal stepped crack in the shear wall, which leads to collapse of wall. Simultaneously, crushing of the toes takes place in compression, see Fig. 13(b). The experimental behaviour and crack pattern obtained are well captured by the proposed composite interface model, which shows that the proposed model is capable of providing the information of the failure analysis of the shear walls.

## 6. Conclusion

A plasticity based composite interface model is proposed, which is capable of simulating the initiation and propagation of crack under combined normal and shear stresses. Moreover, singularity at the corner region is removed by using a single surface yield criteria, which is capable of representing pressure-dependent friction shear failure, cracking by cut-off in tension and crushing by cap-off in compression. The model is developed by integrating the differential equation by fully implicit Euler backward method. The equation are solved by a fully Newton-Raphson technique in monolithic manner, which lead to combined local and global approach. The sub stepping is applied to the model to ensure the convergence and accuracy of the final solution at both local and global level.

First, the model is verified by using basic example i.e. tension, compression and shear. Then, the validation of the model against the experimental results has been carried out on the masonry bed joint in direct shear and the shear wall. The numerical result shows good correlation with experimental result.

## Appendix A. Expression of elasto-plastic interfaces model, first and second derivatives

$$T_1 := [(C - \sigma_{nn}\tan(\phi))] \quad T_2 := [C_Q - \sigma_{nn}\tan(\psi)]$$

$$f_t(\boldsymbol{\sigma}, \boldsymbol{q}) := \frac{2}{\pi}\arctan\left(\frac{\xi - \sigma_{nn}}{\alpha_t}\right) \quad D_t := 1 + \left(\frac{\sigma_{nn} - \xi}{\alpha_t}\right)^2$$

$$f_c(\boldsymbol{\sigma},\boldsymbol{q}) := \frac{2}{\pi}\arctan\left(\frac{\sigma_{nn}-\zeta}{\alpha_c}\right) \quad D_c := 1+\left(\frac{\sigma_{nn}-\zeta}{\alpha_t}\right)^2$$

$$F(\boldsymbol{\sigma},\boldsymbol{q}) := -[(C-\sigma_{nn}\tan(\phi))]^2 f_c f_t + \sigma_{tt}^2$$

$$Q(\boldsymbol{\sigma},\boldsymbol{q}) := -[C_Q-\sigma_{nn}\tan(\psi)]^2 f_c f_t + \sigma_{tt}^2$$

$$\boldsymbol{n} = \begin{bmatrix} 2T_1\tan\phi F_c F_t - T_1^2\left(\frac{2F_c}{\pi\alpha_t D_t}+\frac{2F_t}{\pi\alpha_c D_c}\right) & 2\sigma_{tt}\end{bmatrix}$$

$$\boldsymbol{m} = \begin{bmatrix} 2T_2\tan\psi F_c F_t - T_2^2\left(\frac{2F_c}{\pi\alpha_t D_t}+\frac{2F_t}{\pi\alpha_c D_c}\right) & 2\sigma_{tt}\end{bmatrix}$$

Derivative of $\boldsymbol{m}$

$$T_3 = \frac{F_c}{\pi\alpha_t^3 D_t^2}+\frac{F_t}{\pi\alpha_c^3 D_c^2}+\frac{4}{\pi^2\alpha_t D_t\alpha_c D_c}$$

$$\frac{\partial \mathbf{m}}{\partial \boldsymbol{\sigma}} = \begin{bmatrix} -2\tan^2\psi F_c F_t + 8T_2\tan\psi\left(\frac{F_c}{\pi\alpha_t D_t}+\frac{F_t}{\pi\alpha_c D_c}\right)+2T_2^2T_3 & 0\\ 0 & 2\end{bmatrix}$$

$$\frac{\partial m_1}{\partial \boldsymbol{q}} = \begin{bmatrix} 0\\ 2\tan\psi F_c F_t - 4T_2\left(\frac{F_c}{\pi\alpha_t D_t}+\frac{F_t}{\pi\alpha_c D_c}\right)\\ 0\\ 2\sec^2\psi F_c F_t(T_2-\sigma_{nn}\tan\psi)-2(\sigma_{nn}\sec^2\psi-2T_2)\left(\frac{F_c}{\pi\alpha_t D_t}+\frac{F_t}{\pi\alpha_c D_c}\right)\\ \frac{-4\tan\psi T_2 F_c}{\pi\alpha_t D_t}+4T_2\left(\frac{1}{\pi^2\alpha_c D_c\alpha_t D_t}-\frac{F_c(\sigma-\xi)}{\pi\alpha_t^3 D_t^2}\right)\\ \frac{-4\tan\psi T_2 F_t}{\pi\alpha_c D_c}+4T_2\left(\frac{1}{\pi^2\alpha_c D_c\alpha_t D_t}-\frac{F_c(\sigma-\xi)}{\pi\alpha_c^3 D_c^2}\right)\end{bmatrix}$$

$$\boldsymbol{H} = \begin{bmatrix} \langle\sigma_{nn}\rangle & 0\\ 0 & \sigma_{tt}-\sigma_{t_{r1}}sign(\sigma_{tt})\\ 0 & (\sigma_{tt_{r1}}-\sigma_{tt_{r2}})sign(\sigma_{tt})\\ \langle\langle\sigma_{nn}\rangle\rangle & 0\end{bmatrix}$$

$$\varpi = \begin{bmatrix} \left(-m_1\boldsymbol{H}(1,1)\frac{\beta_c}{G_f^I}-m_2\boldsymbol{H}(2,2)\frac{\beta_c}{G_f^{II}}\right)(C_0-C_r)\exp^{-\beta_c\left(\frac{w_1^p}{G_f^I}+\frac{w_2^p}{G_f^{II}}\right)}\\ \left(-m_1\boldsymbol{H}(1,1)\frac{\beta_{C_Q}}{G_f^I}-m_2\boldsymbol{H}(2,2)\frac{\beta_{C_Q}}{G_f^{II}}\right)(C_{Q_0}-C_{Q_r})\exp^{-\beta_{C_Q}\left(\frac{w_1^p}{G_f^I}+\frac{w_2^p}{G_f^{II}}\right)}\\ -m_2\boldsymbol{H}(3,2)\beta_\phi(\phi_0-\phi_r)\exp^{-\beta_\phi w_3^p}\\ -m_2\boldsymbol{H}(3,2)\beta_\psi(\psi_0-\psi_r)\exp^{-\beta_\psi w_3^p}\\ \left(-m_1\boldsymbol{H}(1,1)\frac{\beta_\xi}{G_f^I}-m_2\boldsymbol{H}(2,2)\frac{\beta_\xi}{G_f^{II}}\right)\xi_0\exp^{-\beta_\xi\left(\frac{w_1^p}{G_f^I}+\frac{w_2^p}{G_f^{II}}\right)}\\ -m_1\boldsymbol{H}(4,1)\frac{\partial\zeta}{\partial w_4}\end{bmatrix}$$

$$\frac{\partial\zeta}{\partial w_4} = \begin{cases} 2(\zeta_p-\zeta_0)\left(\left(\frac{2w_4^p}{w_p}\right)-\left(\frac{w_4^p}{w_p}\right)^2\right)^{-\frac{1}{2}}\left(\frac{2}{w_p}+\frac{2w_4}{w_p^2}\right) & \text{if } w_4^p\leqslant w_p\\ 2(\zeta_m-\zeta_p)\left(\frac{w_4^p-w_p}{(w_m-w_p)^2}\right) & \text{if } w_p\leqslant w_4^p\leqslant w_m\\ \beta_\zeta\exp^{\beta_\zeta\left(\frac{w_4^p-w_p}{\zeta_m-\zeta_r}\right)} & \text{if } w_4^p>w_m\end{cases}$$

## References


[1] Drysdale RG, Hamid AA, Baker LR. Masonry structures: behavior and design. NJ: Englewood Cliffs; 1994.
[2] Hendry AW. Reinforced and prestressed masonry. Longman Scientific & Technical; 1991.
[3] Dhanasekar M, Kleeman PW, Page AW. Biaxial stress–strain relations for brick masonry. J Struct Eng 1985;111(5):1085–100.
[4] Andreaus U. Failure criteria for masonry panels under in-plane loading. J Struct Eng 1996;122(1):37–46.
[5] Page A. The biaxial compressive strength of brick masonry. ICE Proc, vol. 71. Ice Virtual Library; 1981. p. 93–906.
[6] Page A. The strength of brick masonry under biaxial compression-tension. Int J Masonry Construct 1983;3(1):26–31.
[7] Van der Pluijm R. Material properties of masonry and its components under tension and shear. In: Proceedings of the 6th Canadian masonry symposium. Saskatoon, Saskatchevan: University of Saskatchevan; 1992.
[8] Vermeltfoort AT. Compression properties of masonry and its components. In: Proceedings of the 10th international brick and block masonry conference. Calgary, vol. 3; 1994. p. 1433–42.
[9] Vermeltfoort A. Brick-mortar interaction in masonry under pressure. PhD thesis, technical. University of Eindhoven, Eindhoven, NL-NB, Nederland; 2004.
[10] Vermeltfoort AT, Raijmakers TM, Janssen H. Shear tests on masonry walls. In: Hamid AA, Harris HG, editors. Proc. 6th North American masonry conf. Philadelphia, Pennsylvania; 1993. p. 1183–93.
[11] Roca P, González J, Oñate E, Lourenço P. Experimental and numerical issues in the modelling of the mechanical behaviour of masonry. Structural analysis of historical constructions II 1998.
[12] Raijmakers T, Vermeltfoort AT. Deformation controlled tests in masonry shear walls. Report Ba, vol. 1156; 1992.
[13] Goodman RE, Taylor RL, Brekke TL. A model for the mechanics of jointed rock. J Soil Mech Found Div 1968.
[14] Rots JG. Computational modeling of concrete fracture. PhD thesis, Technische Hogeschool Delft; 1988.
[15] Zubelewicz A, Bazant ZP. Interface element modeling of fracture in aggregate composites. J Eng Mech 1987;113(11):1619–30.
[16] Carol I, Prat PC, López CM. Normal/shear cracking model: application to discrete crack analysis. J Eng Mech 1997;123(8):765–73.
[17] Caballero A, Carol I, López C. A meso-level approach to the 3d numerical analysis of cracking and fracture of concrete materials. Fatigue Fract Eng Mater Struct 2006;29(12):979–91.
[18] Citto C. Two-dimensional interface model applied to masonry structures. ProQuest; 2008.
[19] Arya S, Hegemier G. On non-linear response prediction of concrete masonry assemblies. In: Proc. North Am. masonry conf. Masonry Society, Boulder, Colorado; 1978. p. 19.1–24.
[20] Page A. Finite element model for masonry. J Struct Div 1978;104(8):8 1267–1285.
[21] Stankowski T. Numerical simulation of progressive failure in particle composites. PhD thesis, technical. University of Colorado, Boulder, Colorado; 1990.
[22] Stankowski T, Runesson K, Sture S. Fracture and slip of interfaces in cementitious composites. i: Characteristics. J Eng Mech 1993;119(2):292–314.
[23] Lotfi HR. Finite element analysis of fracture of concrete and masonry structures. PhD thesis, University of Colorado; 1992.
[24] Lotfi HR, Shing PB. Interface model applied to fracture of masonry structures. J Struct Eng 1994;120(1):63–80.
[25] Lourenço P. Analysis of masonry structures with interface elements. TNO building and construction research; 1994.
[26] Lourenço P. Computational strategies for masonry structures; 1996.
[27] Lourenço PB, Rots JG. Multisurface interface model for analysis of masonry structures. J Eng Mech 1997;123(7):660–8.
[28] Giambanco G, Rizzo S, Spallino R. Numerical analysis of masonry structures via interface models. Comput Methods Appl Mech Eng 2001;190(49):6493–511.
[29] de Castro Oliveira DV. Experimental and numerical analysis of blocky masonry structures under cyclic loading. PhD thesis, Universidade do Minho; 2003.
[30] Oliveira DV, Lourenço PB. Implementation and validation of a constitutive model for the cyclic behaviour of interface elements. Comput Struct 2004;82(17):1451–61.
[31] Dolatshahi KM, Aref AJ. Two-dimensional computational framework of meso-scale rigid and line interface elements for masonry structures. Eng Struct 2011;33(12):3657–67.
[32] Dhanasekar M, Haider W. Explicit finite element analysis of lightly reinforced masonry shear walls. Comput Struct 2008;86(1):15–26.
[33] Anand SC, Yalamanchili KK. Three-dimensional failure analysis of composite masonry walls. J Struct Eng 1996;122(9):1031–9.
[34] Andreaus U, Ceradini G. Failure modes of solid brick masonry under in-plane loading. Masonry Int 1992;6(1):4–8.
[35] Andreaus U, Ceradini G, Cerone M, D'Asdia P. Masonry columns under horizontal loads: a comparison between finite element modeling and experimental results. In: Proceedings of the 7th international brick and block masonry conference. Melbourne, vol. 1; 1985. p. 469–78.
[36] Andreaus U, Cerone M, D'Asdia P, Lannozzi F. A finite element model for the analysis of masonry structures under cyclic actions. In: Proceedings of the 7th international brick and block masonry conference. Melbourne, vol. 1; 1985. p. 479–88.
[37] Andreaus U, di Paolo A. A 3d finite element model for the analysis of masonry structures. In: Proceedings of the 8th international brick and block masonry conference. Dublin, vol. 3; 1988. p. 1405–16.
[38] Andreaus U, di Paolo A. 3D analysis of masonry columns with grouted reinforcement bars. In: Proceedings of the 8th international brick and block masonry conference. Dublin, vol. 3; 1988. p. 1507–18.
[39] Andreaus U, Ippoliti L. A two storey masonry wall under cyclic loading: a comparison between experimental and numerical results. In: Proceedings of the 3rd international symposium on computer methods in structural masonry. Lisbon, vol. 1; 1995. p. 68–77.
[40] Andreaus U, Ippoliti L. Masonry panel under inplane loading: a comparison between experimental and numerical results. In: Proceedings of the 3rd international symposium on computational methods and experimental measurements. Capri, Italy, vol. 1; 1995. p. 603–10.
[41] Andreaus U, Ippoliti L. A two storey masonry wall under monotonic loading: a comparison between experimental and numerical results. In: Proceedings of the 4th international conference on structural repair and maintenance of historical buildings. Creta, vol. 1; 1995. p. 319–26.
[42] Andreaus U, Ippoliti L. A two storey masonry wall under seismic loading: a comparison between simple and strengthened masonry. In: Proceedings of the

4th international conference on structural repair and maintenance of historical buildings. Creta, vol. 1; 1995. p. 319–26.
[43] Ernesto G, Maura I, Elio S. A beam finite element for nonlinear analysis of masonry elements with or without fiber reinforced plastic reinforcements. Int J Architect Heritage: Conserv Anal Restor 2011;5(6):693–716.
[44] Daniela A, Alessandro M, Elio S. An equilibrated macro element for non linear analysis of masonry structures. Eng Struct 2014;70(1):82–93.
[45] Andrea P, Sergio L, Alessandro G. A nonlinear macro element model for the seismic analysis of masonry buildings. Earthquake Eng Struct Dynam 2014;43(2):159–79.
[46] Brasile S, Casciaro R, Formica G. Finite element formulation for nonlinear analysis of masonry walls. Comput Struct 2010;88(3–4):135–43.
[47] Macorini L, Izzuddin B. Nonlinear analysis of masonry structures using mesoscale partitioned modeling. Adv Eng Softw 2013;60–61(1):58–69.
[48] Macorini L, Izzuddin B. Nonlinear analysis of unreinforced masonry walls unde blast loading using mesoscale partitioned modeling. Adv Eng Softw 2013;60–61(1):58–69.
[49] Koutromanos I, Shing PB. Cohesive crack model to simulate cyclic response of concrete and masonry structures. ACI Struct J 2012;109(3):349–58.
[50] Ehsan M, Franklin LM, Ahmad AH. Nonlinear finite element modeling of reinforced masonry shear walls for bidirectional loading response. Finite Elem Anal Des 2014;84(1):44–53.
[51] Ehsan M, Franklin LM, Ahmad AH. Nonlinear fe analysis of out of plane behaviour of masonry walls with and without cfrp reinforcement. Finite Elem Anal Des 2014;84(1):44–53.
[52] Sarah P, Katrin B. Influence of boundary conditions and size effect on the drift capacity of urm walls. Eng Struct 2014;65(1):76–88.
[53] Gian PL, Andrea P, Gaetano M. Numerical investigation on the influence of frp retrofit layout and geometry on the inplane behavior of masonry walls. ASCE J Compos Construct 2012;16(1):1 712–723.
[54] Ivo C, Massimo M, Bartolomeo P. A new discrete element model for the evaluation of the seismic behaviour of unreinforced masonry buildings. Eng Struct 2012;40(1):327–38.
[55] Amaryllis M, Maria R, Andrea P, Guido M. Identification of suitable limit states from nonlinear dynamic analyses of masonry structures. J Earthquake Eng 2014;18(2):231–63.
[56] Amjad A, Kiarash M. A three dimensional cyclic meso-scale numerical procedure for simulation of unreinforced masonry structures. Comput Struct 2013;120(1):9–23.
[57] Nebojsa M, Neven K, Joseph S. Modeling the behaviour of seismically strengthened masonry walls subjected to cyclic in-plane shear. Eng Struct 2013;56(1):1 1117–1129.
[58] Medeiros P, Vasconcelos G, Lourenco PB, Gouveia J. Numerical modeling of non-confined and confined masonry walls. Construct Build Mater 2013;1:968–76.
[59] Lucia k, Harris M, Panayotis C. Explicit finite element analysis for the in-plane cyclic behavior of unreinforced masonry structures. Earthquake Eng Struct Dynam 2011;40(2):2 175–193.
[60] Manos GC, Soulis VJ, Thauampteh J. The behavior of masonry assemblages and masonry-infilled rc frames subjected to combined vertical and cyclic horizontal seismic type loading. Adv Eng Softw 2012;45(1):213–31.
[61] Subramaniam K, Sinha S. Analytical model for cyclic compressive behavior of brick masonry. ACI Struct J 1995;92(3):288–94.
[62] Viorel P, Radu P, Anderi P. In plane cyclic behavior of masonry walls jacketed with fiber reinforced mortar and fiber grids. Math Model Civil Eng 2013;9(3):32–9.
[63] Ghiassi B, Soltani M, Tasnimi A. A simplified model for analysis of unreinforced masonry shear walls under combined axial, shear and flexural loading. Eng Struct 2012;42:396–409.
[64] Michele Betti AV, Galano Luciano. Comparative analysis on the seismic behavior of unreinforced masonry buildings with flexible diaphragms. Eng Struct 2014;61:195–208.
[65] Rui Marques PBL. Unreinforced and confined masonry buildings in seismic regions: validation of macro element models and cost analysis. Eng Struct 2014;64:52–67.
[66] Sergio Lagomarsino AGSC, Penna Andrea. Tremuri program: an equivalent frame model for the nonlinear seismic analysis of masonry buildings. Eng Struct 2013;56:1787–99.
[67] Kenneth A Gent Franch MAAIREG, Morbelli Gian M Giuliano. A seismic vulnerability index for confined masonry shear wall buildings and a relationship with the damage. Eng Struct 2008;30(10):2605–12.
[68] Verstrynye DVGMHE, Schueremans L. Modeling and analysis of time dependent behavior of historical masonry under high stress loads. Eng Struct 2011;33(1):210–7.
[69] Ivo Calio BP, Marletta Massimo. A new discrete element model for the evaluation of seismic behavior of unreinforced masonry buildings. Eng Struct 2012;40:327–38.
[70] Valdimir G Haach MRSC, Ramalho Marcio A. Parametrical study of unreinforced flayed masonry walls subjected to horizontal loading through numerical modeling. Eng Struct 2013;56:207–17.
[71] Nathalie Domede TS, Sellier Alain. Structural analysis of a multi-span railway masonry bridge combining in-situ observations, laboratory tests and damage modeling. Eng Struct 2013;56:837–49.
[72] Pawan Agnihotri DCR, Singhal Vaibhav. Effect of in-plane damage on out of plane strength of unreinforced masonry walls. Eng Struct 2013;57:1–11.
[73] Monica Puglisi JFL. Maylitt Liz Categui, modeling of masonry of infilled frames part ii: Cracking and damage. Eng Struct 2009;31(1):119–24.
[74] Pereira R. Performance evaluation of masonry in-filled re frames under cyclic loading based on damage methods. Eng Struct 2005;27(8):1278–88.
[75] Siro Casolo GM. A simplified homogenisation-discrete element model for the non-linear static analysis of masonry walls out-of-plane loaded. Eng Struct 2010;32(8):2352–66.
[76] Vincenzo Gattulli GMAP, Lampis Gianluea. Simulations of frp reinforcement in masonry panels and applications to a historic facade. Eng Struct 2014;75:604–618, 201.
[77] Bibiano Luccioni VCR. Numerical analysis of fiber reinforced polymer retrofitted masonry panels. Eng Struct 2013;49:360–72.
[78] Hrvoje Smolijanoisc ZN, Zivaljic Nikolina. A combined finite discrete element analysis of dry stone masonry structures. Eng Struct 2013;52:89–100.
[79] Daniela Addesi ES, Mastrandrea Alessandro. An equilibrated macro-element for non-linear analysis of masonry structures. Eng Struct 2014;70(a):82–93.
[80] Giamundo GLYSGMV, Sarhosis V. Evaluation of different computational modeling strategies for the analysis of low strength masonry structures. Eng Struct 2014;73:160–9.
[81] Shahid Nazir D, Manicka. Modeling the failure of thin layered mortar joints in masonry. Eng Struct 2013;49:615–27.
[82] Van der Pluijm R, Rutten H, Ceelen M. Shear behaviour of bed joints. In: 12th Int. brick/block masonry conf. proc., vol. 3; 2000. p. 1849–62.
[83] Atkinson R, Amadei B, Saeb S, Sture S. Response of masonry bed joints in direct shear. J Struct Eng 1989;115(9):2276–96.
[84] Simo J, Hughes T. Computational inelasticity, local iteration at global iteration max. Ave. max. ave. unified non-unified, vol. 6. New York: Springer; 1989 (4.5).
[85] Zienkiewicz OC, Taylor RL, Zhu JZ. The finite element method: its basis and fundamentals 1. Butterworth-Heinemann; 2005.
[86] Niels SO, Matti R. The mechanics of constitutive modeling; 2005.
[87] ABAQUS V. 6.9 online documentation, SIMULIA Inc; 2009.
[88] Pérez-Foguet A, Rodrıguez-Ferran A, Huerta A. Consistent tangent matrices for substepping schemes. Comput Methods Appl Mech Eng 2001;190(35):4627–47.
[89] Wang W, Datcheva M, Schanz T, Kolditz O. A sub-stepping approach for elasto-plasticity with rotational hardening. Comput Mech 2006;37(3):266–78.
[90] Caballero A, Willam K, Carol I. Consistent tangent formulation for 3d interface modeling of cracking/fracture in quasi-brittle materials. Comput Methods Appl Mech Eng 2008;197(33):2804–22.
[91] Vermeltfoort AT, Raijmakers T. Deformation controlled tests in masonry shear walls, part 2. Tech. rep., Report TUE/BKO/93.08, Eindhoven University of Technology, Eindhoven, The Netherlands; 1993.